

# Evaluation of probabilistic photometric redshift estimation approaches for LSST

S.J. Schmidt<sup>1</sup>, A.I. Malz<sup>2,3,4</sup>, J.Y.H. Soo<sup>5</sup>, I.A. Almosallam<sup>6,7</sup>, M. Brescia<sup>8</sup>, S. Cavaudi<sup>8,9</sup>, J. Cohen-Tanugi<sup>10</sup>, A.J. Connolly<sup>11</sup>, P.E. Freeman<sup>12</sup>, M.L. Graham<sup>11</sup>, K. Iyer<sup>13</sup>, M.J. Jarvis<sup>14,15</sup>, J.B. Kalmbach<sup>16</sup>, E. Kovacs<sup>17</sup>, A.B. Lee<sup>12</sup>, G. Longo<sup>9</sup>, C. B. Morrison<sup>11</sup>, J. Newman<sup>18</sup>, E. Nourbakhsh<sup>1</sup>, E. Nuss<sup>10</sup>, T. Pospisil<sup>12</sup>, H. Tranin<sup>10</sup>, R. Zhou<sup>18</sup>, R. Izbicki<sup>19,20</sup>

(LSST Dark Energy Science Collaboration)

<sup>1</sup> Department of Physics, University of California, One Shields Ave., Davis, CA, 95616, USA

<sup>2</sup> German Centre of Cosmological Lensing, Ruhr-Universitaet Bochum, Universitaetsstrasse 150, 44801 Bochum, Germany

<sup>3</sup> Center for Cosmology and Particle Physics, New York University, 726 Broadway, New York, 10003, USA

<sup>4</sup> Department of Physics, New York University, 726 Broadway, New York, 10003, USA

<sup>5</sup> Department of Physics and Astronomy, University College London, Gower Street, London WC1E 6BT, UK

<sup>6</sup> King Abdulaziz City for Science and Technology, Riyadh 11442, Saudi Arabia

<sup>7</sup> Information Engineering, Parks Road, Oxford, OX1 3PJ, UK

<sup>8</sup> INAF-Capodimonte Observatory, Salita Moiariello 16, I-80131, Napoli, Italy

<sup>9</sup> Department of Physics E. Pancini, University Federico II, via Cinthia 6, I-80126, Napoli, Italy

<sup>10</sup> Laboratoire Univers et Particules de Montpellier, Université de Montpellier, CNRS, Montpellier, France

<sup>11</sup> Department of Astronomy, University of Washington, Box 351580, U.W., Seattle WA 98195, USA

<sup>12</sup> Department of Statistics & Data Science, Carnegie Mellon University, 5000 Forbes Avenue, Pittsburgh, PA 15213, USA

<sup>13</sup> Department of Physics and Astronomy, Rutgers, The State University of New Jersey, 136 Frelinghuysen Road, Piscataway, NJ 08854-8019 USA

<sup>14</sup> Astrophysics, Department of Physics, University of Oxford, Denys Wilkinson Building, Keble Road, Oxford, OX1 3RH, UK

<sup>15</sup> Department of Physics and Astronomy, University of the Western Cape, Bellville 7535, South Africa

<sup>16</sup> Department of Physics, University of Washington, Box 351560, Seattle, WA 98195, USA

<sup>17</sup> Argonne National Laboratory, Lemont, IL 60439, USA

<sup>18</sup> Department of Physics and Astronomy and the Pittsburgh Particle Physics, Astrophysics and Cosmology Center (PITT PACC), University of Pittsburgh, Pittsburgh, PA 15260, USA

<sup>19</sup> Department of Statistics, Federal University of Sao Carlos, Sao Carlos, Brazil

<sup>20</sup> External collaborator

10 October 2019

## ABSTRACT

Many scientific investigations of photometric galaxy surveys require redshift estimates, whose uncertainty properties are best encapsulated by photometric redshift (photo- $z$ ) posterior probability distribution functions (PDFs). A plethora of photo- $z$  PDF estimation methodologies abound, producing discrepant results with no consensus on a preferred approach. We present the results of a comprehensive experiment comparing twelve photo- $z$  algorithms applied to mock data produced for the Large Synoptic Survey Telescope (LSST) Dark Energy Science Collaboration (DESC). By supplying perfect prior information, in the form of the complete template library and a representative training set as inputs to each code, we demonstrate the impact of the assumptions underlying each technique on the output photo- $z$  PDFs. In the absence of a notion of true, unbiased photo- $z$  PDFs, we evaluate and interpret multiple metrics of the ensemble properties of the derived photo- $z$  PDFs as well as traditional reductions to photo- $z$  point estimates. We report systematic biases and overall over/under-breadth of the photo- $z$  PDFs of many popular codes, which may indicate avenues for improvement in the algorithms or implementations. Furthermore, we raise attention to the limitations of established metrics for assessing photo- $z$  PDF accuracy; though we identify the conditional density estimate (CDE) loss as a promising metric of photo- $z$  PDF performance in the case where true redshifts are available but true photo- $z$  PDFs are not, we emphasize the need for science-specific performance metrics.

**Key words:** galaxies: distances and redshifts – galaxies: statistics – methods: statistical

## 2 LSST Dark Energy Science Collaboration

### 1 INTRODUCTION

The current and next generations of large-scale galaxy surveys, including the Dark Energy Survey (DES, Abbott et al. 2005), the Kilo-Degree Survey (KiDS, de Jong et al. 2013), Hyper Suprime-Cam Survey (HSC, Aihara et al. 2018a,b), Large Synoptic Survey Telescope (LSST, Abell et al. 2009), Euclid (Laureijs et al. 2011), and Wide-Field Infrared Survey Telescope (WFIRST, Green et al. 2012), represent a paradigm shift to reliance on photometric, rather than solely spectroscopic, galaxy catalogues of substantially larger size at a cost of lacking complete spectroscopically confirmed redshifts ( $z$ ). Effective astrophysical inference using the catalogues resulting from these ongoing and upcoming missions, however, necessitates accurate and precise photometric redshift (photo- $z$ ) estimation methodologies.

As an example, in order for photo- $z$  systematics to not dominate the statistical noise floor of LSST’s main cosmological sample of  $\sim 10^7$  galaxies, the LSST Science Requirements Document (SRD)<sup>1</sup> specifies that individual galaxy photo- $zs$  must have root-mean-square error  $\sigma_z < 0.02(1+z)$ ,  $3\sigma$  catastrophic outlier rate below 10%, and bias below 0.003. Specific science cases may have their own requirements on photo- $z$  performance that exceed those of the survey as a whole. In that vein, the LSST Dark Energy Science Collaboration (LSST-DESC) developed a separate SRD (The LSST Dark Energy Science Collaboration et al. 2018) that conservatively forecasts the constraining power of five cosmological probes, leading to even more stringent requirements on photo- $z$  performance, including those defined in terms of tomographically binned subsamples populations rather than individual galaxies.

Though the standard has long been for each galaxy in a photometric catalogue to have a photo- $z$  point estimate and Gaussian error bar, even early applications of photo- $zs$  in precision cosmology indicate the inadequacy of point estimates (Mandelbaum et al. 2008) to encapsulate the degeneracies resulting from the nontrivial mapping between broad band fluxes and redshift. Far from a hypothetical situation, such degeneracies are real consequences of the same deep imaging that enables larger galaxy catalogue sizes. The lower luminosity and higher redshift populations captured by deeper imaging introduce major physical systematics to photo- $zs$ , among them the Lyman break/Balmer break degeneracy, that did not affect shallower large area surveys like the Sloan Digital Sky Survey (SDSS, York et al. 2000) and Two Micron All Sky Survey (2MASS, Skrutskie et al. 2006).

To fully characterize such physical degeneracies, later photometric galaxy catalogue data releases, (e. g. Sheldon et al. 2012; Erben et al. 2013; de Jong et al. 2017), provide a more informative photo- $z$  data product, the photo- $z$  probability density function (PDF), that describes the redshift probability, commonly denoted as  $p(z)$ , as a function of a galaxy’s redshift, conditioned on the observed photometry. Early template-based methods such as Fernández-Soto et al. (1999) approximated the likelihood of photometry conditioned on redshift with the relative  $\chi^2$  values of template

spectra. Not long after, Bayesian adaptations of template-based approaches such as Benítez (2000) combined the estimated likelihoods with a prior to yield a posterior PDF of redshift conditioned on photometry. While the first data-driven photo- $z$  algorithms yielded a point estimate, Firth et al. (2003) estimated a photo- $z$  PDF using a neural net with realizations scattered within the photometric errors.

There are numerous techniques for deriving photo- $z$  PDFs, yet no one method has been established as clearly superior. Consistent experimental conditions enable the quantification if not isolation of their differences, which can be interpreted as a sort of *implicit prior* imparted by the method itself. Comprehensive comparisons of photo- $z$  methods have been made before; the Photo- $z$  Accuracy And Testing (PHAT, Hildebrandt et al. 2010) effort focused on photo- $z$  point estimates derived from many photometric bands. Rau et al. (2015) introduced a new method for improving photo- $z$  PDFs using an ordinal classification algorithm. DES compared several codes for photo- $z$  point estimates and a subset with photo- $z$  PDF information (Sánchez et al. 2014) and examined summary statistics of photo- $z$  PDFs for tomographically binned galaxy subsamples (Bonnett et al. 2016).

This paper is distinguished from other comparisons of photo- $z$  methods by its focus on the evaluation criteria for photo- $z$  PDFs and interpretation thereof. In the absence of simulated data drawn from known redshift distributions, the very concept of a “true PDF” for an individual galaxy is unavailable, and we must instead rely on measures of ensemble behaviour to characterize PDF quality (see § 4 for further discussion). We aim to perform a comprehensive sensitivity analysis of photo- $z$  PDF techniques in order to ultimately select those that will become part of the LSST pipelines, as part of a key project of the Photometric Redshifts working group of the LSST-DESC, described in the Science Roadmap (SRM)<sup>2</sup>. In this initial study, we focus on evaluating the performance of photo- $z$  PDF codes using PDF-specific performance metrics in a formally controlled experiment with complete and representative prior information (template libraries and training sets) to set a baseline for subsequent investigations. This approach probes how each code considered exploits the information content of the data versus prior information from template libraries and training sets.

The outline of the paper is as follows: in § 2 we present the simulated data set; in § 3 we describe the current generation codes employed in the paper; in § 4 we discuss the interpretation of photo- $z$  PDFs in terms of metrics of accuracy; in § 5 we show our results and compare the performance of the codes; in § 6 we offer our conclusions and discuss future extensions of this work.

### 2 DATA

In order to test the current generation of photo- $z$  PDF codes, we employ an existing simulated galaxy catalogue, described in detail in Section 2.1. The experimental conditions shared

<sup>1</sup> available at <https://docushare.lsstcorp.org/docushare/dsweb/Get/LPM-17>

<sup>2</sup> Available at: [http://lsst-desc.org/sites/default/files/DESC\\_SRMs\\_V1\\_1.pdf](http://lsst-desc.org/sites/default/files/DESC_SRMs_V1_1.pdf)

among all codes are motivated by the LSST SRD requirements and implemented for machine learning and template-based photo- $z$  PDF codes according to the procedures of Sections 2.3.1 and 2.3.2 respectively.

## 2.1 The Buzzard-v1.0 simulation

Our mock catalogue is derived from the BUZZARD-highres-v1.0 catalogue (DeRose et al. 2019, Wechsler et al., in prep.). BUZZARD is built on a dark matter-only N-body simulation of  $2048^3$  particles in a  $400 \text{ Mpc h}^{-1}$  box. The lightcone was constructed from smoothing and interpolation between a set of time snapshots. Dark matter halos were identified using the Rockstar software package (Behroozi et al. 2013) and then populated with galaxies with a stellar mass and absolute  $r$ -band magnitude in the SDSS system determined using a sub-halo abundance matching model constrained to match both projected two-point galaxy clustering statistics and an observed conditional stellar mass function (Reddick et al. 2013).

To assign a spectrum to each galaxy, the Adding Density Dependent Spectral Energy Distributions (SEDs) procedure (ADDSEDS, deRose in prep.)<sup>3</sup> was used. ADDSEDS uses a sample of  $\sim 5 \times 10^5$  galaxies from the magnitude-limited SDSS Data Release 6 Value Added Galaxy Catalogue (Blanton et al. 2005) to train an empirical relation between absolute  $r$ -band magnitude, local galaxy density, and SED. Each SDSS spectrum is parameterized by five weights corresponding to a weighted sum of five basis SED components using the k-correct software package<sup>4</sup> (Blanton & Roweis 2007).

Correlations between SED and galaxy environment were included so as to preserve the colour-density relation of galaxy environment. The distance to the spatially projected fifth-nearest neighbour was used as a proxy for local density in the SDSS training sample. For each simulated galaxy, a galaxy with similar absolute  $r$ -band magnitude and local galaxy density was chosen from the training set, and that training galaxy's SED was assigned to the simulated galaxy.

### 2.1.1 Caveats

By necessity, BUZZARD does not contain all of the complicating factors present in real data, and here we discuss the most pertinent ways that these limitations affect our experiment. BUZZARD includes only galaxies, not stars nor AGN. The catalogue-based construction excludes image-level effects, such as deblending errors, photometric measurement issues, contamination from sky background (Zodiacal light, scattered light, etc.), lensing magnification, and Galactic reddening.

The BUZZARD SEDs are drawn from a set of  $\sim 5 \times 10^5$  SEDs, which themselves are derived from a five-component linear combination fit to  $\sim 5 \times 10^5$  SDSS galaxies; thus the sample contains only galaxies that resemble linear combinations of those for which SDSS obtained spectra, and there are necessarily duplicates. The linear combination SEDs also restrict the properties of the galaxy population to linear combinations of the properties corresponding to five basis

templates, precluding the modeling of non-linear features such as the full range of emission line fluxes relative to the continuum. The only form of intrinsic dust reddening comes from what is already present in the five basis SEDs via the training set used to create the basis templates, and linear combinations thereof do not span the full range of realistic dust extinction observed in galaxy populations.

While these idealized conditions limit the realism of our mock data, they are irrelevant to the controlled experimental conditions of this study, if anything assuring that differentiation in the performance of the photo- $z$  PDF codes is due to the inferential techniques rather than nuances in the data.

## 2.2 LSST-like mock observations

Given the SED, absolute  $r$ -band magnitude, and true redshift of each simulated galaxy, we computed apparent magnitudes in the six LSST filter passbands,  $ugrizy$ . We assigned magnitude errors in the six bands using the simple model of Ivezić et al. (2008), assuming achievement of the full 10-year depth, with a modification of fiducial LSST total numbers of 30-second visits for photometric error generation: we assume 60 visits in  $u$ -band, 80 visits in  $g$ -band, 180 visits in  $r$ -band, 180 visits in  $i$ -band, 160 visits in  $z$ -band, and 160 visits in  $y$ -band.

As a consequence of adding Gaussian-distributed photometric errors, 2.0% of our galaxies exhibit a negative flux in one or more bands, the vast majority of which are in the  $u$ -band. We deem such negative fluxes *non-detections* and assign a placeholder magnitude of 99.0 in the catalogue to indicate to the photo- $z$  PDF codes that such galaxies would be “looked at but not seen” in multi-band forced photometry.

The full dataset thus covers 400 square degrees and contains 238 million galaxies of redshift  $0 < z \leq 8.7$  down to  $r = 29$ . Systematic inconsistencies with galaxy colors at  $z > 2$  were observed, so the catalogue was limited to  $0 < z \leq 2.0$ . To obtain a catalogue matching the LSST Gold Sample, we imposed an cut of  $i < 25.3$ , which gives a signal-to-noise ratio  $\gtrsim 30$  for most galaxies. In order for statistical errors to be subdominant to the systematic errors we aim to probe, we further reduced the sample size to  $< 10^7$  galaxies by isolating  $\sim 16.8$  square degrees selected from five separate spatial regions of the simulation. We refer to this final set of galaxies as DC1, for the first LSST-DESC Data Challenge.

## 2.3 Shared prior information

For the purpose of performing a controlled experiment that compares photo- $z$  PDF codes on equal footing as a baseline for a future sensitivity analysis, we take care to provide each with maximally optimistic prior information. Redshift estimation approaches built upon physical modeling and machine learning alike have a notion of prior information considered beyond the photometry of the data for which redshift is to be constrained: that information is derived from a template library for a model-based code and a training set for a data-driven code. In this initial study, we seek to set a baseline for a later comparison of the performance of photo- $z$  PDF codes under incomplete and non-representative prior

<sup>3</sup> <https://github.com/vipasu/addsed>

<sup>4</sup> <http://kcorrect.org>

## 4 LSST Dark Energy Science Collaboration

information that will propagate differently in the space of data-driven and model-based algorithms. However, for the baseline case of perfect prior information, physical modeling and machine learning codes can indeed be put on truly equal footing. We outline the equivalent ways of providing all codes perfect prior information below.

### 2.3.1 Training and test set division

Following the findings of Bernstein & Huterer (2010), Masters et al. (2017) that only  $10^4$  spectra are necessary to calibrate photo-zs to Stage IV requirements, we aimed to set aside a randomly selected training set of  $3 - 5 \times 10^4$  galaxies,  $\sim 10\%$  of the full sample. After all cuts described above, we designated the *DC1 training set* of 44 404 galaxies for which observed photometry, true SEDs, and true redshifts would be provided to all codes and the blinded *DC1 test set* of 399 356 galaxies for which photometry alone would be provided to all codes and photo-z PDFs would be requested. The exact form of LSST photometric filter transmission curves were also considered public information that could be used by any code.

### 2.3.2 Template library construction

We aimed to provide template-fitting codes with complete yet manageable library of templates spanning the space of SEDs of the DC1 galaxies. We constructed  $K = 100$  representative templates from the  $\sim 5 \times 10^5$  SEDs of the SDSS DR6 NYU-VAGC by using the five-dimensional vectors of SED weight coefficients described above. After regularizing the SED weight coefficients  $\in [0, 1]$ , we ran a simple K-means clustering algorithm on the five-dimensional space of regularized SED weight coefficients of the SDSS galaxy sample. The resulting clusters were used to define Voronoi cells in the space of weight coefficients, with centre positions corresponding to weights for the k-correct SED components, yielding the 100 SEDs that comprise the *DC1 template set* provided to all template-based codes. We did not, however, exclude from consideration template-based codes that made modifications in their use of these templates due to architecture limitations (as opposed to knowledge of the experimental conditions that could artificially boost the code's apparent performance), with deviations noted in Section 3.

## 3 METHODS

Here we summarize the twelve photo-z PDF codes compared in this study, also in Table 1, which include both established and emerging approaches in template fitting and machine learning. Though not exhaustive, this sample represents codes for which there was sufficient expertise within the LSST-DESC Photometric Redshifts Working Group. Some aspects of data treatment were left to the individual code runners, for example, whether/how to split the available data with known redshifts into separate training and validation sets.

Another key difference is the treatment of non-detections in one or more bands: some codes ignore incomplete bands, while others replace the value with either an estimate for the detection limit, the mean of other values in

the training set, or another default value. There are varying conventions among machine learning based codes for treatment of non-detections, and no one prescription dominates in the photo-z literature. However, we remind the reader that only 2.0 per cent of our sample has non-detections, almost exclusively in the *u*-band, and thus should not dominate the code performance differences.

The authors welcome interest from those outside LSST-DESC to have their codes assessed in future investigations that build upon this one.

We describe the algorithms and implementations of the model-based and data-driven codes in Sections 3.1 and 3.2 respectively, with a straw-person approach included in Section 3.3.

### 3.1 Template-based Approaches

We test three publicly available and commonly used template-based codes that share the standard physically motivated approach of calculating model fluxes for a set of template SEDs on a grid of redshift values and evaluating a  $\chi^2$  merit function using the observed and model fluxes:

$$\chi^2(z, T, A) = \sum_i^{N_{\text{filt}}} \left( \frac{F_{\text{obs}}^i - A F_{\text{pred}}^i(T, z)}{\sigma_{\text{obs}}^i} \right)^2 \quad (1)$$

where  $A$  is a normalization factor,  $F_{\text{pred}}^i(T, z)$  is the flux predicted for a template  $T$  at redshift  $z$ ,  $F_{\text{obs}}^i$  is the observed flux in a given band  $i$ ,  $\sigma_{\text{obs}}^i$  is the observed flux error, and  $N_{\text{filt}}$  is the total number of filters, in our case the six *ugrizy* LSST filters. The likelihood is a sum of observed flux error  $\sigma_b^{\text{obs}}$ -weighted squared differences between the observed flux  $F_b^{\text{obs}}$  and the normalized predicted flux  $F_b^{\text{mod}}(T, z)$  in  $N_{\text{filt}}$  photometric filters  $b$ , which is the LSST *ugrizy* filters in this case. Specific implementation details of each code, e. g. prior form and implementation, are described below.

#### 3.1.1 BPZ

Bayesian Photometric Redshift (BPZ<sup>5</sup>, Benítez 2000) determines the likelihood  $p(C|z, T)$  of a galaxy's observed colours  $C$  for a set of SED templates  $T$  at redshifts  $z$ . The BPZ likelihood is related to the  $\chi^2$  likelihood by  $p(C|z, T) \propto \exp[-\chi^2/2]$ . Given a Bayesian prior  $p(z, T|m_0)$  over apparent magnitude  $m_0$  and type  $T$ , and assuming that the SED templates are spanning and exclusive, BPZ constructs the redshift posterior  $p(z|C, m_0)$  by marginalizing over all SED templates with the form  $p(z|C, m_0) \propto \sum_T p(C|z, T) p(z, T|m_0)$  (Eq. 3 from Benítez 2000), corresponding to setting the parameter PROBS\_LITE=TRUE in the BPZ parameter file. The BPZ prior is the product of an SED template proportion that varies with apparent magnitude  $p(T|m_0)$  and a prior  $p(z|T, m_0)$  over the expected redshift as a function of apparent magnitude and SED template. We anticipate BPZ to outperform other template-based approaches due to the prior that both comprehensively accounts for SED type and is calibrated to the training set.

Here we test BPZ-v 1.99.3 (Benítez 2000) with the DC1

<sup>5</sup> <http://www.stsci.edu/~dcoe/BPZ/>

**Table 1.** List of photo-z PDF codes featured in this study

Published code	Type	Public source code
LePhare (Arnouts et al. 1999)	template fitting	<a href="http://www.cfht.hawaii.edu/~arnouts/lephare.html">http://www.cfht.hawaii.edu/~arnouts/lephare.html</a>
BPZ (Benítez 2000)	template fitting	<a href="http://www.stsci.edu/~dcoe/BPZ/">http://www.stsci.edu/~dcoe/BPZ/</a>
EAZY (Brammer et al. 2008)	template fitting	<a href="https://github.com/gbrammer/eazy-photoz">https://github.com/gbrammer/eazy-photoz</a>
ANNz2 (Sadeh et al. 2016)	machine learning	<a href="https://github.com/IftachSadeh/ANNZ">https://github.com/IftachSadeh/ANNZ</a>
FlexZBoost (Izbicki & Lee 2017)	machine learning	<a href="https://github.com/tospis/i/flexcode">https://github.com/tospis/i/flexcode</a> ; <a href="https://github.com/rizbicki/FlexCoDE">https://github.com/rizbicki/FlexCoDE</a>
GPz (Almosallam et al. 2016b)	machine learning	<a href="https://github.com/OxfordML/GPz">https://github.com/OxfordML/GPz</a>
METAPhR (Cavuoti et al. 2017)	machine learning	<a href="http://dame.dsfs.unina.it">http://dame.dsfs.unina.it</a>
CMNN (Graham et al. 2018)	machine learning	N/A
SkyNet (Graff et al. 2014)	machine learning	<a href="http://ccforge.cse.rl.ac.uk/gf/project/skynet/">http://ccforge.cse.rl.ac.uk/gf/project/skynet/</a>
TPZ (Carrasco Kind & Brunner 2013)	machine learning	<a href="https://github.com/mgckind/MLZ">https://github.com/mgckind/MLZ</a>
Delight (Leistedt & Hogg 2017)	hybrid	<a href="https://github.com/ixkael/Delight">https://github.com/ixkael/Delight</a>
trainZ	machine learning	See Section 3.3

329 template set of Section 2.3.2. To keep the number of free pa-  
 330 rameters manageable, the DC1 template set is pre-sorted by  
 331 the rest-frame  $u - g$  colour and split into three broad classes  
 332 of SED template, equivalent to the E, Sp and Im/SB types.  
 333 The Bayesian prior term  $p(T|m_0)$  was derived directly from  
 334 the DC1 training set, and the other term  $p(z|T, m_0)$  was  
 335 chosen to be the best fit for the eleven free parameters from  
 336 the functional form of Benítez (2000). We use template in-  
 337 terpolation, creating two linearly interpolated templates be-  
 338 tween each basis SED (sorted by rest-frame  $u - g$  colour) by  
 339 setting the parameter `INTERP=2`. Prior to running the code,  
 340 the non-detection placeholder magnitude was replaced with  
 341 an estimate of the one- $\sigma$  detection limit for the undetected  
 342 band as a proxy for a value close to the estimated sky noise  
 343 threshold.

### 3.1.2 EAZY

344 Easy and Accurate Photometric Redshifts from Yale (EAZY<sup>6</sup>,  
 345 Brammer et al. 2008) extends the basic  $\chi^2$  fit procedure that  
 346 defines template-fitting approaches. The algorithm models  
 347 the observed photometry with a linear combination of tem-  
 348 plate SEDs at each redshift. The best-fit SED at each red-  
 349 shift is found by simultaneously fitting one, two, or all of  
 350 the templates via  $\chi^2$  minimization, which is distinct from  
 351 marginalizing across all templates. The minimized  $\chi^2$  like-  
 352 lihood at each redshift is then combined with an apparent  
 353 magnitude prior to obtain the redshift posterior PDF. We  
 354 note that the utilization of the best-fit SED conditioned on  
 355 redshift rather than a proper marginalization does not lead  
 356 to the correct posterior distribution, an implementation is-  
 357 sue that has now been identified and will be addressed by  
 358 the developers in the future.

359 In contrast with BPZ, EAZY’s apparent magnitude prior is  
 360 independent of SED, though it was derived empirically from  
 361 the DC1 training set. The EAZY architecture cannot accept  
 362 a template set other than the same five basis templates em-  
 363 ployed by `k-correct` when constructing the DC1 catalogue,  
 364 but, for consistency with the experimental scope of perfect  
 365 prior information, EAZY’s flexible `all-templates` mode was  
 366 used to fit the photometric data with a linear combination  
 367 of the five basis templates. Though EAZY can account for  
 368 uncertainty in the template set by adding in quadrature to  
 369 the flux errors an empirically derived template error as a

371 function of redshift, we set the template error to zero since  
 372 the same templates were in fact used to produce the DC1  
 373 photometry.

### 3.1.3 LePhare

374 Photometric Analysis for Redshift Estimate (LePhare<sup>7</sup>,  
 375 Arnouts et al. 1999; Ilbert et al. 2006) uses the  $\chi^2$  of Equa-  
 376 tion 1 to match observed colors with those predicted from a  
 377 template set. The template set can be semi-empirical or en-  
 378 tirely synthetic. The reported photo-z PDF is an arbitrary  
 379 normalization of the likelihood evaluated on the output red-  
 380 shift grid.

381 Here we use LePhare-v 2.2 with the DC1 template set  
 382 of Section 2.3.2. Unlike both BPZ and EAZY, LePhare uses  
 383 generic, SED-independent priors that are not tuned to the  
 384 DC1 data set.

## 3.2 Machine Learning-based Approaches

386 We compared nine data-driven photo-z estimation ap-  
 387 proaches, eight of which are described in this section and one  
 388 of which is discussed in Section 3.3. Because the algorithms  
 389 differ more from one another and the techniques are rela-  
 390 tive newcomers to the astronomical literature, we provide  
 391 somewhat more detail about the implementations below.

### 3.2.1 ANNz2

394 ANNz2<sup>8</sup> (Sadeh et al. 2016) supports several machine learn-  
 395 ing algorithms, including artificial neural networks (ANN),  
 396 boosted decision tree, and k-nearest neighbour (KNN) re-  
 397 gression. In addition to accounting for errors on the input  
 398 photometry, ANNz2 uses the KNN-uncertainty estimate of  
 399 Oyaizu et al. (2008) to quantify uncertainty in the choice of  
 400 method over multiple runs. Using the Toolkit for Multivariate  
 401 Data Analysis with ROOT<sup>9</sup>, ANNz2 can return the results  
 402 of running a single machine learning algorithm, a “best”  
 403 choice of the results from simultaneously running multiple  
 404 algorithms (based on evaluation the cumulative distribution  
 405 functions of validation set objects), or a combination of the

<sup>7</sup> <http://www.cfht.hawaii.edu/~arnouts/lephare.html>

<sup>8</sup> <https://github.com/IftachSadeh/ANNZ>

<sup>9</sup> <http://tmva.sourceforge.net/>

<sup>6</sup> <https://github.com/gbrammer/eazy-photoz>

## 6 LSST Dark Energy Science Collaboration

406 results of multiple algorithms weighted by their method uncertainties averaged over multiple runs.

407 In this study, we used ANNz2-v.2.0.4 to output only the result of the ANN algorithm. Photo-z PDFs were produced  
 408 by running an ensemble of 5 ANNs with a 6 : 12 : 12 : 1  
 409 architecture corresponding to the 6 *ugrizy* inputs, 2 hidden  
 410 layers with 12 nodes each, and 1 output of redshift. Each of  
 411 the five ANNs was trained with different random seeds for  
 412 the initialization of input parameters, reserving half of the  
 413 training set for validation to prevent overfitting. Undetected  
 414 galaxies were excluded from the training set, and per-band  
 415 non-detections in the test set were replaced with the mean  
 416 magnitude in that band within the entire test set.  
 417

### 419 3.2.2 Colour-Matched Nearest-Neighbours

420 The colour-matched nearest-neighbours photometric red-  
 421 shift estimator (CMNN, [Graham et al. 2018](#)) uses a training  
 422 set of galaxies with known redshifts that has equivalent or  
 423 better photometry than the test set in terms of quality and  
 424 filter coverage. For each galaxy in the test set, CMNN identifies  
 425 a colour-matched subset of training galaxies using a thresh-  
 426 old in the Mahalanobis distance  $D_M = \sum_j^{N_{\text{colours}}} (c_j^{\text{train}} -$   
 $c_j^{\text{test}})^2 / \delta c_{\text{test}}^2$  in the space of available colours  $c$ , with colour  
 427 measurement errors  $\delta c_{\text{test}}$  and  $N_{\text{colours}} = 5$  colors  $j$  defined  
 428 by the *ugrizy* filters, which defines the set of colour-matched  
 429 neighbours based on a value of the percent point function  
 430 (PPF). As an example, for  $N_{\text{fit}} = 5$  with PPF = 0.95, 95%  
 431 of all training galaxies consistent with the test galaxy will  
 432 have  $D_M < 11.07$ . Undetected bands are dropped, thereby  
 433 reducing the effective  $N_{\text{fit}}$  for that galaxy. The photo-z PDF  
 434 of a given test set galaxy is the normalized distribution of  
 435 redshifts of its colour-matched subset of training set galax-  
 436 ies.  
 437

438 Here, we make two modifications to the implementation  
 439 of [Graham et al. \(2018\)](#) to comply with the controlled exper-  
 440 imental conditions. First, we do not impose non-detections  
 441 on galaxies fainter than the expected LSST 10-year limit-  
 442 ing magnitude nor galaxies bright enough to saturate with  
 443 LSST’s CCDs, instead using all of the photometry for the  
 444 DC1 test and training sets. Second, we apply the initial  
 445 colour cut to the training set before calculating the Ma-  
 446 halanobis distance in order to accelerate processing and use a  
 447 magnitude pseudo-prior as in [Graham et al. \(2018\)](#), but for  
 448 both we use cut-off values corresponding to the DC1 training  
 449 set galaxies’ colours and magnitudes.

450 We make an additional adaptation to enable the CMNN  
 451 algorithm to yield accurate photo-z PDFs for all galaxies,  
 452 as the original [Graham et al. \(2018\)](#) algorithm is optimized  
 453 for photo-z point estimates and is susceptible to less ac-  
 454 curate photo-z PDFs for bright galaxies or those with few  
 455 matches in colour-space. We use PPF = 0.95 rather than  
 456 PPF = 0.68 to generate the subset of colour-matched train-  
 457 ing galaxies, whose redshifts are weighted by their inverse  
 458 Mahalanobis distances of the when composing the photo-  
 459 z PDF rather than weighting all colour-matched training  
 460 galaxies equally. Additionally, when the number of colour-  
 461 matched training set galaxies is less than 20, the nearest 20  
 462 neighbours in color-space are used instead, and the output  
 463 photo-z PDF is convolved with a Gaussian kernel of vari-

464 ance  $\sigma_{\text{train}}^2 (\text{PPF}_{20} / 0.95)^2 - 1$  to account for the correspond-  
 465 ing growth of the effective PPF to include 20 neighbors.

### 466 3.2.3 Delight

467 [Delight](#)<sup>10</sup> ([Leistedt & Hogg 2017](#)) is a hybrid technique that  
 468 infers photo-zs with a data-driven model of latent SEDs and  
 469 a physical model of photometric fluxes as a function of red-  
 470 shift. Generally, machine learning methods rely on represen-  
 471 tative training data with shared photometric filters, while  
 472 template based methods rely on a complete library of tem-  
 473 plates based on physical models constructed. [Delight](#) aims  
 474 to take the best aspects of both approaches by construct-  
 475 ing a large collection of latent SED templates (or physical  
 476 flux-redshift models) from training data, with a template  
 477 SED library as a guide to the learning of the model, thereby  
 478 circumventing the machine learning prerequisite of represen-  
 479 tative training data in the same photometric bands and the  
 480 template fitting requirement of detailed galaxy SED models.  
 481 It models noisy observed flux  $\hat{\mathbf{F}} = \mathbf{F} + F_b$  as a sum of a noise-  
 482 less flux plus a Gaussian processes  $F_b \sim \mathcal{GP}(\mu^F, k^F)$  with  
 483 zero mean function  $\mu^F$  and a physically motivated kernel  $k^F$   
 484 that induces realistic correlations in flux-redshift space.

485 From a template-fitting perspective, each test set galaxy  
 486 has a posterior  $p(z|\hat{\mathbf{F}}) \approx \sum_i p(\hat{\mathbf{F}}|z, T_i)p(z|T_i)p(T_i)$  of red-  
 487 shift  $z$  conditioned on noisy flux  $\hat{\mathbf{F}}$ , where  $p(z|T_i)p(T_i)$  cap-  
 488 tures prior information about the redshift distributions and  
 489 abundances of the galaxy templates  $T_i$ . As in traditional  
 490 template fitting, each likelihood  $p(\hat{\mathbf{F}}|\mathbf{F})$  relates the noisy flux  
 491  $\hat{\mathbf{F}}$  with the noiseless flux  $\mathbf{F}$  predicted by the model of a linear  
 492 combination of templates, carefully constructed to account  
 493 for model uncertainties and different normalization of the  
 494 same SED, plus the Gaussian process term.

495 The machine learning approach appears in the inclu-  
 496 sion of a pairwise comparison term  $p(\mathbf{F}|z, z_j, \hat{\mathbf{F}}_j)$  for the  
 497 prediction of model flux  $\mathbf{F}$  at a model redshift  $z$  with re-  
 498 spect to training set galaxy  $j$  with redshift  $z_j$  and ob-  
 499 served flux  $\hat{\mathbf{F}}_j$ . Thus the photo-z posterior  $p(\hat{\mathbf{F}}|z, T_i) =$   
 $\int p(\hat{\mathbf{F}}|\mathbf{F})p(\mathbf{F}|z, z_j, \hat{\mathbf{F}}_j)d\mathbf{F}$  may be interpreted as the proba-  
 $500$   
 $501$   
 $502$   
 $503$   
 $504$   
 $505$   
 $506$   
 $507$   
 $508$   
 $509$   
 $510$   
 $511$   
 $512$   
 $513$   
 $514$   
 $515$   
 $516$

500 probability that the training and the target galaxies have the same  
 501 SED at different redshifts. The flux prediction  $p(\mathbf{F}|z, z_j, \hat{\mathbf{F}}_j)$   
 502 of the training galaxy at redshift  $z$  is modeled via the Gaus-  
 503 sian process described above; more detail is provided in  
 $504$   
 $505$   
 $506$   
 $507$   
 $508$   
 $509$   
 $510$   
 $511$   
 $512$   
 $513$   
 $514$   
 $515$   
 $516$

[Leistedt & Hogg \(2017\)](#).

506 In this study, the default settings of [Delight](#) were used,  
 507 with the exception that the PDF bins were set to be linearly-  
 508 spaced rather than logarithmic. The Gaussian process was  
 509 trained using the full DC1 training set. We used the full DC1  
 510 template set with a flat prior in magnitude and SED type.  
 511 Photometric uncertainties from the inputs are propagated  
 512 into the code, while non-detections for each band are set to  
 513 the mean of the respective bands.

### 514 3.2.4 FlexZBoost

515 [FlexZBoost](#)<sup>11</sup> ([Izbicki & Lee 2017](#)) is built on [FlexCode](#), a  
 516 general-purpose methodology for converting any conditional

<sup>10</sup> <https://github.com/ixkael/Delight>

<sup>11</sup> <https://github.com/tpospisi/flexcode>;  
<https://github.com/rizbicki/FlexCoDE>

mean point estimator of  $z$  to a conditional density estimator  $p(z|\mathbf{x}) \equiv f(z|\mathbf{x})$ , where  $\mathbf{x}$  here represents our photometric covariates and errors. **FlexZBoost** expands the unknown function  $f(z|\mathbf{x}) = \sum_i \beta_i(\mathbf{x})\phi_i(z)$  using an orthonormal basis  $\{\phi_i(z)\}_i$ . By the orthogonality property, the expansion coefficients  $\beta_i(\mathbf{x}) = \mathbb{E}[\phi_i(z)|\mathbf{x}] \equiv \int f(z|\mathbf{x})\phi_i(z)dz$  are thus conditional means. The expectation value  $\mathbb{E}[\phi_i(z)|\mathbf{x}]$  of the expansion coefficients conditioned on the data is equivalent to the regression of the space of possible redshifts on the space of possible photometry. Thus the expansion coefficients  $\beta_i(\mathbf{x})$  can be estimated from the data via regression to yield the conditional density estimate  $\hat{f}(z|\mathbf{x})$ .

In this paper, we used **xgboost** (Chen & Guestrin 2016) for the regression; it should, however, be noted that **FlexCode-RF**<sup>11</sup>, based on Random Forests, generally performs better on smaller datasets. As our basis  $\phi_i(z)$ , we choose a standard Fourier basis. The two tuning parameters in our photo- $z$  PDF estimate are the number  $I$  of terms in the series expansion and an exponent  $\alpha$  that we use to sharpen the computed density estimates  $\hat{f}(z|\mathbf{x}) \propto \hat{f}(z|\mathbf{x})^\alpha$ . Both  $I$  and  $\alpha$  were chosen in an automated way by minimizing the weighted  $L_2$ -loss function (Eq. 5 in Izbicki & Lee 2017) on a validation set comprised of a randomly selected 15% of the DC1 training set. While **FlexCode**'s lossless native encoding stores each photo- $z$  PDF using the basis coefficients  $\beta_i(\mathbf{x})$ , we discretized the final estimates into 200 linearly-spaced redshift bins  $0 < z < 2$  to match the consistent output format of the experimental conditions.

### 545 3.2.5 GP<sub>z</sub>

546 GP<sub>z</sub><sup>12</sup> (Almosallam et al. 2016a,b) is a sparse Gaussian process based code, a scalable approximation of full Gaussian Processes (Rasmussen & Williams 2006), that produces input-dependent variance estimates corresponding to 547 heteroscedastic noise. The model assumes a Gaussian posterior probability  $p(z|\mathbf{x}) = \mathcal{N}(z|\mu(\mathbf{x}), \sigma(\mathbf{x})^2)$  of the 548 output redshift  $z$  given the input photometry  $\mathbf{x}$ . The mean 549  $\mu(\mathbf{x})$  and the variance  $\sigma(\mathbf{x})^2$  are modeled as functions 550  $f(\mathbf{x}) = \sum_{i=1}^m w_i \phi_i(\mathbf{x})$  linear combinations of  $m$  basis 551 functions  $\{\phi_i(\mathbf{x})\}_{i=1}^m$  with associated weights  $\{w_i\}_{i=1}^m$ . The 552 details on how to learn the parameters of the model and the 553 hyper-parameters of the basis functions are described in Al- 554 mosallam et al. (2016b). GP<sub>z</sub>'s variance estimate is composed 555 of a model uncertainty term corresponding to sparsity of the 556 training set photometry and a noise uncertainty term en- 557 compassing noisy photometric observations, enabling quan- 558 tification of any need for more representative or more precise 559 training samples. GP<sub>z</sub> may also weight training set samples 560 by importance according to  $|z_{\text{spec}} - z_{\text{phot}}|/(1+z_{\text{spec}})$  to min- 561 imize the normalized photo- $z$  point estimate error, however, 562 this function may be adapted to photo- $z$  PDFs, pressuring 563 the model to dedicate more resources to test set galaxies 564 that are not well-represented in the training set.

To smooth the long tail in the distribution of magnitude errors, we use the log of the magnitude errors, im- 570 proving numerical stability and eliminating the need for 571 constraints on the optimization process. Unobserved mag- 572 nitudes  $x_u = \mu_u + \Sigma_{uo}\Sigma_{oo}^{-1}(x_o - \mu_o)$  were imputed from

573 observed magnitudes  $x_o$  and the training set mean  $\mu$  and 574 covariance  $\Sigma$  using a linear model. This is the optimal ex- 575 pected value of the unobserved variables given the observed 576 ones under the assumption that the distribution is jointly 577 Gaussian; note that this reduces to a simple average if the 578 covariates are independent with  $\Sigma_{uo} = 0$ . We reserved for 579 validation 20% of the training set and used the Variable 580 Covariance option in GP<sub>z</sub> with 200 basis functions (see Al- 581 mosallam et al. (2016b) for details), neglecting to apply cost- 582 sensitive learning options.

### 584 3.2.6 METAPhōR

585 Machine-learning Estimation Tool for Accurate Photomet- 586 ric Redshifts (METAPhōR<sup>13</sup>, Cavuoti et al. 2017) is based on 587 the Multi Layer Perceptron with Quasi Newton Algorithm 588 (MLPQNA) with the least square error model and Tikhonov 589  $L_2$ -norm regularization (Hofmann & Mathé 2018). Photo- $z$  590 PDFs are generated by running  $N$  trainings on the same 591 training set, or  $M$  trainings on  $M$  different random sam- 592 plings of the training set. Upon regression of the test set, 593 the photometry  $m_{ij}$  of each test set galaxy  $j$  in filter  $i$  is 594 perturbed according to  $m'_{ij} = m_{ij} + \alpha_i F_{ij} \epsilon$  in terms of 595 the standard normal random variable  $\epsilon \sim \mathcal{N}(0, 1)$ , a mul- 596 tiplicative constant  $\alpha_i$  permitting accommodation of multi- 597 survey photometry, and a bimodal function  $F_{ij}$  composed of 598 a polynomial fit of the mean magnitude errors on the binned 599 bands plus a constant term representing the threshold below 600 which the polynomial's noise contribution is negligible 601 (Brescia et al. 2018).

602 In this work, we used a hierarchical KNN to replace 603 non-detections with values based on their neighbors. The 604 usual cross-validation of redshift estimates and PDFs was 605 also omitted for this study.

### 606 3.2.7 SkyNet

607 SkyNet<sup>14</sup> (Graff et al. 2014) employs a neural network based 608 on a second order conjugate gradient optimization scheme 609 (see Graff et al. 2014, for further details). The neural net- 610 work is configured as a standard multilayer perceptron with 611 three hidden layers and one input layer with 12 nodes cor- 612 responding to the 6 photometric magnitudes and their mea- 613 surement errors.

614 SkyNet's classifier mode uses a cross-entropy error func- 615 tion with a 20:40:40 node (all rectified linear units) architec- 616 ture for each hidden layer and an output layer of 200 nodes 617 corresponding to 200 bins for the PDF, with a softmax acti- 618 vation function to enforce the normalization condition that 619 the probabilities sum to unity. While previous implemen- 620 tations of the code (see Appendix C.3 of Sánchez et al. 2014; 621 Bonnett 2015) implement a sliding bin smoothing, no such 622 procedure was used in this study.

623 We pre-whitened the data by pegging the magnitudes 624 to (45,45,40,35,42,42) and errors to (20,20,10,5,15,15) for 625 ugrizy filters, respectively. To avoid over-fitting, 30% of the 626 training set was reserved for validation, and training was 627 halted as soon as the error rate began to increase on the

<sup>12</sup> <https://github.com/OxfordML/GPz>

<sup>13</sup> <http://dame.dsfa.unina.it>

<sup>14</sup> <http://ccpforge.cse.rl.ac.uk/gf/project/skynet/>

## 8 LSST Dark Energy Science Collaboration

validation set. The weights were randomly initialized based on normal sampling.

### 3.2.8 TPZ

Trees for Photo- $z$ (TPZ<sup>15</sup>, Carrasco Kind & Brunner 2013; Carrasco Kind & Brunner 2014) uses prediction trees and random forest techniques to estimate photo- $z$  PDFs. TPZ recursively splits the training set into branch pairs based on maximizing information gain among a random subsample of features, to minimize correlation between the trees, terminating only when a newly created leaf meets a criterion, such as a leaf size minimum or a variance threshold. The regions in each terminal leaf node correspond to a subsample of the training set with similar properties. Bootstrap samples from the training set photometry and errors are used to build a set of prediction trees.

To run TPZ, we replaced non-detections with an approximation of the  $1\sigma$  detection threshold based on the error forecast of the 10-year LSST data, i. e.  $dm = 2.5 \log(1 + N/S)$  where  $dm \sim 0.7526$  magnitudes for  $N/S = 1$ . We calibrated TPZ with the Out-of-Bag cross-validation technique (Breiman et al. 1984; Carrasco Kind & Brunner 2013) to evaluate its predictive validity and determine the relative importance of the different input attributes. We grew 100 trees to a minimum leaf size of 5 using the *ugri* magnitudes, all  $u - g, g - r, r - i, i - z, z - y$  colours, and the associated errors, as the  $z$  and  $y$  magnitudes did not show significant correlation with the redshift in our cross-validation. We partitioned our redshift space into 200 bins and smoothed each individual PDF with a smoothing scale of twice the bin size.

### 3.3 trainZ: a pathological photo- $z$ PDF estimator

We also consider a pathological photo- $z$  PDF estimation method, dubbed **trainZ**, which assigns each test set galaxy a photo- $z$  PDF equal to the normalized redshift distribution  $N(z)$  of the training set, according to

$$p(z|\{z_j\}) \equiv \frac{1}{N_{\text{train}}} \sum_{i=1}^{N_{\text{train}}} \begin{cases} 1 & \text{if } z_k \leq z_i < z_{k+1} \\ 0 & \text{otherwise} \end{cases}. \quad (2)$$

Unlike the other methods, the **trainZ** estimator is *independent of the photometric data*, effectively performing a KNN procedure with  $k = N_{\text{train}}$ .

Though **trainZ** is strongly vulnerable to a nonrepresentative training set, it should optimize performance metrics probing the ensemble properties of the galaxy sample, modulo Poisson error due to small sample size, as the training set and test set are drawn from the same underlying population. We will demonstrate its performance under the metrics of Section 4 and discuss it as an illustrative experimental control case in Section 6.1 to highlight the limitations of our evaluation criteria for photo- $z$  PDFs.

## 4 ANALYSIS

The goal of this study is to evaluate the degree to which photo- $z$  PDFs of each method can be trusted for a generic

analysis. The overloaded “ $p(z)$ ” is a widespread abuse of notation that obfuscates this goal, so we dedicate attention to dismantling it here. Galaxies have redshifts  $z$  and photometric data  $d$  drawn from a joint probability space  $p(z, d)$  in nature. As a result, each observed galaxy  $i$  has a *true posterior photo- $z$  PDF*  $p(z|d_i)$  as well as a true likelihood  $p(d|z_i)$ . There are a number of metrics that can be used to test the accuracy of a photo- $z$  posterior as an estimator of a true photo- $z$  posterior if the true photo- $z$  PDF is known. However, the true photo- $z$  PDF is in general not accessible unless the photometry is in fact drawn from a ground truth for the joint probability density of redshift and photometry  $p(z, d)$ . In contrast, existing mock catalogs produce redshift-photometry pairs  $(z, d)$  by a deterministic algorithm that does not correspond to a joint probability density from which one can take samples. In these cases there is no “true PDF” for an individual object, and most measures of PDF fidelity will necessarily be restricted to probing the quality of the ensemble of photo- $z$  PDFs. (See §6.2 for a discussion of how one might circumvent this limitation.)

Before describing the metrics appropriate to the DC1 data set, we outline the philosophy behind our choices. A photo- $z$  PDF estimator derived by method  $H$  must be understood as a posterior probability distribution

$$\hat{p}_i^H(z) \equiv p(z|d_i, I_D, I_H), \quad (3)$$

conditioned not only on the photometric data  $d_i$  for that galaxy but also on parameters encompassing prior information  $I_D$  shared, in our experiment, among all photo- $z$  PDF codes and  $I_H$  that will differ depending on the method  $H$  used to produce it. To be concrete,  $I_D$  takes the form of a training set for the machine learning codes and a template library for the model fitting codes.

The interpretation of the information  $I_H$  is more subtle. This investigation is built upon the knowledge that two codes taking the same approach, among choices of model fitting or machine learning, are nonetheless expected to yield different results even if they take the same external prior information  $I_D$ .  $I_H$  represents the projection of the code’s architecture onto the estimated posteriors over redshift, specific to each code, and even the tunable parameters or random seeds of a specific run of a code with a random component. We thus refer to  $I_H$  as the *implicit prior*, in contrast with the training set or template library provided to a given code explicitly by the researcher.

The presence of the implicit prior in some sense makes a direct comparison of photo- $z$  PDFs produced by different methods impossible; even if they share the same external prior information  $I_D$ , by definition they cannot be conditioned on the same assumptions  $I_H$ , otherwise they would not be distinct methods at all. In this study, we isolate the effect of differences in prior information  $I_H$  specific to each method by using a single training set  $I_D^{\text{ML}}$  for all machine learning-based codes and a single template library  $I_D^T$  for all template-based codes. These sets of prior information are carefully constructed to be representative and complete, so we have  $I_D \equiv I_D^{\text{ML}} \equiv I_D^T$  for every method  $H$ . Under this assumption, a ratio of posteriors of codes is in effect a ratio of the implicit posteriors  $p(z|d_i, I_H')$  since the external prior information  $I_D$  is present in the numerator and denominator. Thus comparisons of  $\hat{p}_i^H(z)$  isolate the effect of the method used to obtain the estimator, which should enable

<sup>15</sup> <https://github.com/mgckind/MLZ>

interpretation of the differences between estimated PDFs in terms of the specifics of the method implementations.

The exact implementation of the metrics theoretically depends on the parametrization of the photo- $z$  PDFs, which may differ across codes and can affect the precision of the estimator (Malz et al. 2018). Even considering a single method under the same parametrization, such as the 200-bin  $0 < z < 2$  piecewise constant function used here, the exact bin definitions must affect the result. The piecewise constant format is chosen because of its established presence in the literature, and the choice of 200 bins was motivated by the approximate number of columns expected to be available for storage of photo- $z$  PDFs for the final LSST Project tables.<sup>16</sup> We will discuss the choice of photo- $z$  PDF parameterization further in Section 6.

This analysis is conducted using the `qp`<sup>17</sup> software package (Malz & Marshall 2018) for manipulating and calculating metrics of univariate PDFs. We present the metrics of photo- $z$  PDFs that address our goals in the sections below. Section 4.1 outlines aggregate metrics of a catalogue of photo- $z$  PDFs, and Section 4.2 presents a metric of individual photo- $z$  PDFs in the absence of true photo- $z$  PDFs. Though the outmoded practices should not be encouraged, those seeking a connection to previous comparison studies will find metrics of redshift point estimate reductions of photo- $z$  PDFs in Appendix B and metrics of a science-specific summary statistics heuristically derived from photo- $z$  PDFs in Appendix A.

## 4.1 Metrics of photo- $z$ PDF ensembles

Because LSST’s photo- $z$  PDFs will be used for many scientific applications, some of which require accuracy of each individual catalog entry, we consider several metrics that probe the population-level performance of the photo- $z$  PDFs. As we have the true redshifts but not true photo- $z$  PDFs for comparison, we remind the reader of the Cumulative Distribution Function (CDF)

$$\text{CDF}[f, q] \equiv \int_{-\infty}^q f(z) dz, \quad (4)$$

of a generic univariate PDF  $f(z)$ , which is used as the basis for several of our metrics. We describe metrics based on the CDF in Section 4.1.1 and metrics of summary statistics thereof in Section 4.1.2.

### 4.1.1 CDF-based metrics

A quantile of a distribution is the value  $q$  at which the CDF of the distribution is equal to  $Q$ ; percentiles and quartiles are familiar examples of linearly spaced sets of 100 and 4 quantiles, respectively. The quantile-quantile (QQ) plot serves as a graphical visualization for comparing two distributions, where the quantiles of one distribution are plotted against the quantiles of the other distribution, providing an intuitive way to qualitatively assess the consistency between an estimated distribution and a true distribution. The closer

the QQ plot is to diagonal, the closer the match between the distributions.

The probability integral transform (PIT)

$$\text{PIT} \equiv \text{CDF}[\hat{p}, z_{\text{true}}] \quad (5)$$

is the CDF of a photo- $z$  PDF evaluated at its true redshift, and the distribution of PIT values probes the average accuracy of the photo- $z$  PDFs of an ensemble of galaxies. The distribution of PIT values is effectively the derivative of the QQ plot. A catalogue of accurate photo- $z$  PDFs should have a PIT distribution that is uniform  $U(0, 1)$ , and deviations from flatness are interpretable: overly broad photo- $z$  PDFs induce underrepresentation of the lowest and highest PIT values, whereas overly narrow photo- $z$  PDFs induce overrepresentation of the lowest and highest PIT values. Catastrophic outliers with a true redshift outside the support of its photo- $z$  PDF have  $\text{PIT} \approx 0$  or  $\text{PIT} \approx 1$ .

The PIT distribution has been used to quantify the performance of photo- $z$  PDF methods in the past (e. g. Borodoloi et al. 2010; Polsterer et al. 2016; Tanaka et al. 2018). Tanaka et al. (2018) use the histogram of PIT values as a diagnostic indicator of overall code performance, while Freeman et al. (2017) independently define the PIT and demonstrate how its individual values may be used both to perform hypothesis testing (via, e. g. the KS, CvM, and AD tests; see below) and to construct quantile-quantile plots. Following Kodra & Newman (in prep.) we define the PIT-based catastrophic outlier rate as the fraction of galaxies with  $\text{PIT} < 0.0001$  or  $\text{PIT} > 0.9999$ , which should total 0.0002 for an ideal uniform distribution.

### 4.1.2 Summary statistics of CDF-based metrics

We evaluate a number of quantitative metrics derived from the visually interpretable QQ plot and PIT histogram, built on the Kolmogorov-Smirnov (KS) statistic

$$\text{KS} \equiv \max_z \left( | \text{CDF}[\hat{f}, z] - \text{CDF}[\tilde{f}, z] | \right), \quad (6)$$

interpretable as the maximum difference between the CDFs of an approximating univariate distribution  $\hat{f}(z)$  and a reference distribution  $\tilde{f}(z)$ , in this case  $U(0, 1)$ . We also consider two variants of the KS statistic. A cousin of the KS statistic, the Cramer-von Mises (CvM) statistic

$$\text{CvM}^2 \equiv \int_{-\infty}^{+\infty} (\text{CDF}[\hat{f}, z] - \text{CDF}[\tilde{f}, z])^2 d\text{CDF}[\tilde{f}, z] \quad (7)$$

is the mean-squared difference between the CDFs of an approximate and true PDF. The Anderson-Darling (AD) statistic

$$\text{AD}^2 \equiv N_{\text{tot}} \int_{-\infty}^{+\infty} \frac{(\text{CDF}[\hat{f}, z] - \text{CDF}[\tilde{f}, z])^2}{\text{CDF}[\tilde{f}, z](1 - \text{CDF}[\tilde{f}, z])} d\text{CDF}[\tilde{f}, z] \quad (8)$$

is a weighted mean-squared difference featuring enhanced sensitivity to discrepancies in the tails of the distribution. In anticipation of a substantial fraction of galaxies having PIT of 0 or 1, a consequence of catastrophic outliers, we evaluate the AD statistic with modified bounds of integration (0.01, 0.99) to exclude those extremes in the name of numerical stability.

<sup>16</sup> See, e. g. the LSST Data Products Definition Document, available at: <https://ls.st/dpdd>

<sup>17</sup> <http://github.com/aimalz/qp/>

842    **4.2 Conditional Density Estimate (CDE) Loss: a  
843    metric of individual photo- $z$  PDFs**

844    The BUZZARD simulation process precludes testing the de-  
845    gree to which samples from our photo- $z$  posteriors recon-  
846    struct the space of  $p(z, \text{data})$ . To the knowledge of the au-  
847    thors, there is only one metric that can be used to evaluate  
848    the performance of individual photo- $z$  PDF estimators in the  
849    absence of true photo- $z$  posteriors. The conditional density  
850    estimation (CDE) loss is an analogue to the familiar root-  
851    mean-square-error used in conventional regression, defined  
852    as

853    
$$L(f, \hat{f}) \equiv \int \int (f(z|\mathbf{x}) - \hat{f}(z|\mathbf{x}))^2 dz dP(\mathbf{x}), \quad (9)$$

854    where  $f(z|\mathbf{x})$  is the true photo- $z$  PDF that we do not have  
855    and  $\hat{f}(z|\mathbf{x})$  is an estimate thereof, in terms of the photom-  
856    etry  $\mathbf{x}$ . (See Section 3.2.4 for a review of the notation.) We  
857    estimate the CDE loss via

858    
$$\hat{L}(f, \hat{f}) = \mathbb{E}_{\mathbf{X}} \left[ \int \hat{f}(z | \mathbf{X})^2 dz \right] - 2\mathbb{E}_{\mathbf{X}, Z} \left[ \hat{f}(Z | \mathbf{X}) \right] + K_f, \quad (10)$$

859    where the first term is the expectation value of the photo- $z$   
860    posterior with respect to the marginal distribution of the  
861    photometric covariates  $\mathbf{X}$ , the second term is the expecta-  
862    tion value with respect to the joint distribution of  $\mathbf{X}$  and the  
863    space  $Z$  of all possible redshifts, and the third term  $K_f$  is  
864    a constant depending only upon the true conditional densi-  
865    ties  $f(z|\mathbf{x})$ . We may estimate these expectations empirically  
866    on the test or validation data (Eq. 7 in Izbicki et al. 2017)  
867    without knowledge of the true densities.

868    **5 RESULTS**

869    We begin with a demonstrative visual inspection of the  
870    photo- $z$  PDFs produced by each code for individual galaxies.  
871    Figure 1 shows the photo- $z$  PDFs for four galaxies chosen  
872    as examples of photo- $z$  PDF archetypes: a narrow unimodal  
873    PDF, a broad unimodal PDF, a bimodal PDF, and a mul-  
874    timodal PDF. We reiterate that under our idealized experi-  
875    mental conditions, differences between codes are the isolated  
876    signature of the implicit prior due to the method by which  
877    the photo- $z$  PDFs were derived.

878    The most striking differences between codes are the  
879    small-scale features induced by the interaction between the  
880    shared piecewise constant parameterization of 200 bins  $0 <$   
881     $z < 2$  of Section 4 and the smoothing conditions or lack  
882    thereof in each algorithm. The  $dz = 0.01$  redshift resolu-  
883    tion is sufficient to capture the broad peaks of faint galax-  
884    ies' photo- $z$  PDFs with large photometric errors but is too  
885    broad to resolve the narrow peaks for bright galaxies' photo-  
886     $z$  PDFs with small photometric errors. This observation is  
887    consistent with the findings of Malz et al. (2018) that the  
888    piecewise constant parameterization underperforms in the  
889    presence of small-scale structures.

890    However, the shared small-scale features of ANNz2,  
891    METAPhoR, CMNN, and SkyNet are a result of various weighted  
892    sums of the limited number of training set galaxies with  
893    colors similar to those of the test set galaxy in question,  
894    with behavior closer to classification than regression in the  
895    case of ANNz2. The settings used on GPz in this work forced

**Table 2.** The catastrophic outlier rate as defined by extreme PIT values. We expect a value of 0.0002 for a proper Uniform distribution. An excess over this small value indicates true redshifts that fall outside the non-zero support of the  $p(z)$ .

Photo- $z$ Code	fraction $\text{PIT} < 10^{-4}$ or $> 0.999$
ANNz2	0.0265
BPZ	0.0192
Delight	0.0006
EAZY	0.0154
FlexZBoost	0.0202
GPz	0.0058
LePhare	0.0486
METAPhoR	0.0229
CMNN	0.0034
SkyNet	0.0001
TPZ	0.0130
trainZ	0.0002

896    broadening of the single Gaussian to cover the multimodal  
897    redshift solutions of the other codes.

898    **5.1 Performance on photo- $z$  PDF ensembles**

899    The histogram of PIT values, QQ plot, and QQ difference  
900    plot relative to the ideal diagonal are provided in Figure 2,  
901    showcasing the biases and trends in the average accuracy  
902    of the photo- $z$  PDFs for each code. The high QQ values  
903    (i. e. more high than low PIT values) of BPZ, CMNN, Delight,  
904    EAZY, and GPz indicate photo- $z$  PDFs biased low, and the  
905    low QQ values (more low than high PIT values) of SkyNet  
906    and TPZ indicate photo- $z$  PDFs biased high. The gray shaded  
907    band marks the  $2\sigma$  variance in PIT values found using the  
908    trainZ algorithm with a bootstrap resampling of the training  
909    set and a sample size of 30,000 galaxies, representing  
910    a very conservative estimate of the representative training  
911    sample size, and thus an approximate minimal error signifi-  
912    cance compared to ideal performance. Deviations in the PIT  
913    histograms outside of this range show that significant biases  
914    are present for some codes.

915    The PIT histograms of Delight, CMNN, SkyNet, and TPZ  
916    feature an underrepresentation of extreme values, indicative  
917    of overly broad photo- $z$  PDFs, while the overrepresentation  
918    of extreme values for METAPhoR indicate overly narrow photo-  
919     $z$  PDFs. These five codes in particular have a free parameter  
920    for bandwidth, which may be responsible for this vulnera-  
921    bility, in spite of the opportunity for fine-tuning with per-  
922    fect prior information. FlexZBoost's "sharpening" parame-  
923    ter (described in Section 3.2.4) played a key role in diagonal-  
924    izing the QQ plot, indicating a common avenue for improve-  
925    ment in the approaches that share this type of parameter.  
926    On the other hand, the three purely template-based codes,  
927    BPZ, EAZY, and LePhare, do not exhibit much systematic  
928    broadening or narrowing, which may indicate that complete  
929    template coverage effectively defends from these effects.

930    Close inspection of the extremes at PIT values of 0 and 1  
931    reveal spikes in the first and last bin of the PIT histogram for  
932    some codes in Figure 2, corresponding to catastrophic out-  
933    liers where the true redshift lies outside of the support of the  
934     $p(z)$ . The catastrophic outlier rates are provided in Table 2.  
935    As expected, trainZ achieves precisely the 0.0002 value ex-

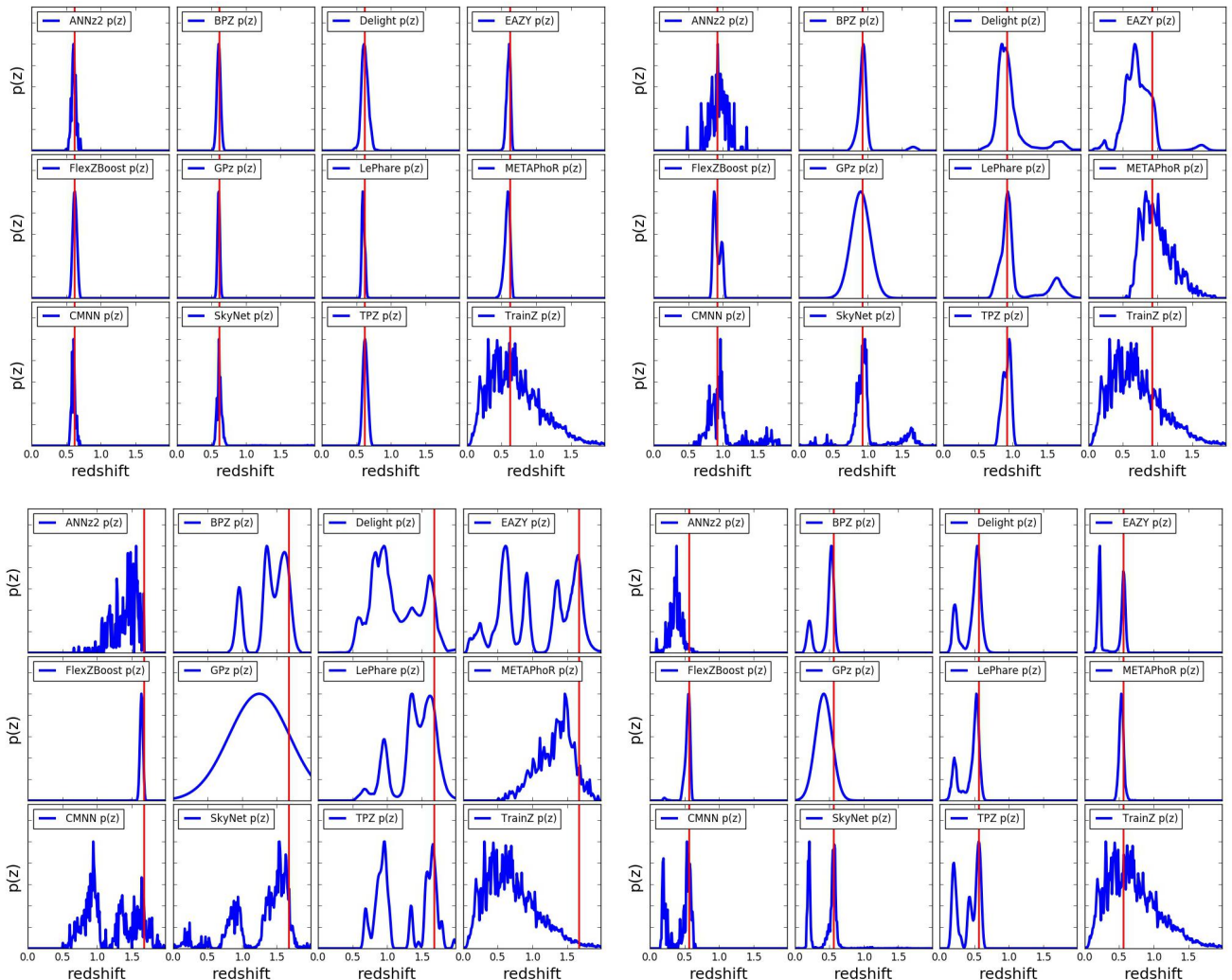


**Figure 1.** The individual photo- $z$  PDFs (blue) distributions produced by the twelve codes (small panels) on four exemplary galaxies' photometry (large panels) with different true redshifts (red). The photo- $z$  PDFs of all codes share some features for the example galaxies due to physical color degeneracies and photometric errors: tight unimodal  $p(z)$  (upper left), broad unimodal  $p(z)$  (upper right), bimodal  $p(z)$  (lower right), and complex/multimodal  $p(z)$  (lower left). The diverse algorithms and implementations induce differences in small-scale structure and sensitivity to physical systematics.

pected of an ideal PIT distribution. ANNz2, FlexZBoost, LePhare, and METAPhoR have notably high catastrophic outlier rates  $> 0.02$ , exceeding 100 times the ideal PIT rate, meriting further investigation.

Figure 3 highlights the relative values of the KS, CvM, and AD test statistics calculated by comparing the PIT distribution and a uniform distribution  $U(0, 1)$ . METAPhoR and LePhare perform well under the AD but poorly under the KS and CvM due to their high catastrophic outlier rates. ANNz2 and FlexZBoost are the top scorers under these metrics of the PIT distribution. ANNz2's strong performance can be attributed to an aspect of the training process in which training set galaxies with a PIT that more closely matches the percentiles of the DC1 training set's redshift distribution are upweighted; in effect, these quantile-based metrics were part of the algorithm itself that may or may not serve it well under more realistic experimental conditions. Similar to what was done for the PIT histograms in Figure 2, we

create bootstrap training samples of 30,000 galaxies for use with `trainZ` in order to estimate a conservative statistical floor that we would expect in real data. No code reaches this idealized floor, indicating that all codes suffer some degradation from the ideal when employing their implicit priors, though ANNz2, FlexZBoost, and GPz are within a factor of two.

## 5.2 Performance on individual photo- $z$ PDFs

The values of the CDE loss statistic of individual photo- $z$  PDF accuracy are provided in Table 3. It is worth noting that strong performance on the CDE loss, corresponding to lower values of the metric, should imply strong performance on the other metrics, though the inverse is not necessarily true. Thus the CDE loss is the most effective metric for generic science cases.

Of the metrics we were able to consider in this experi-

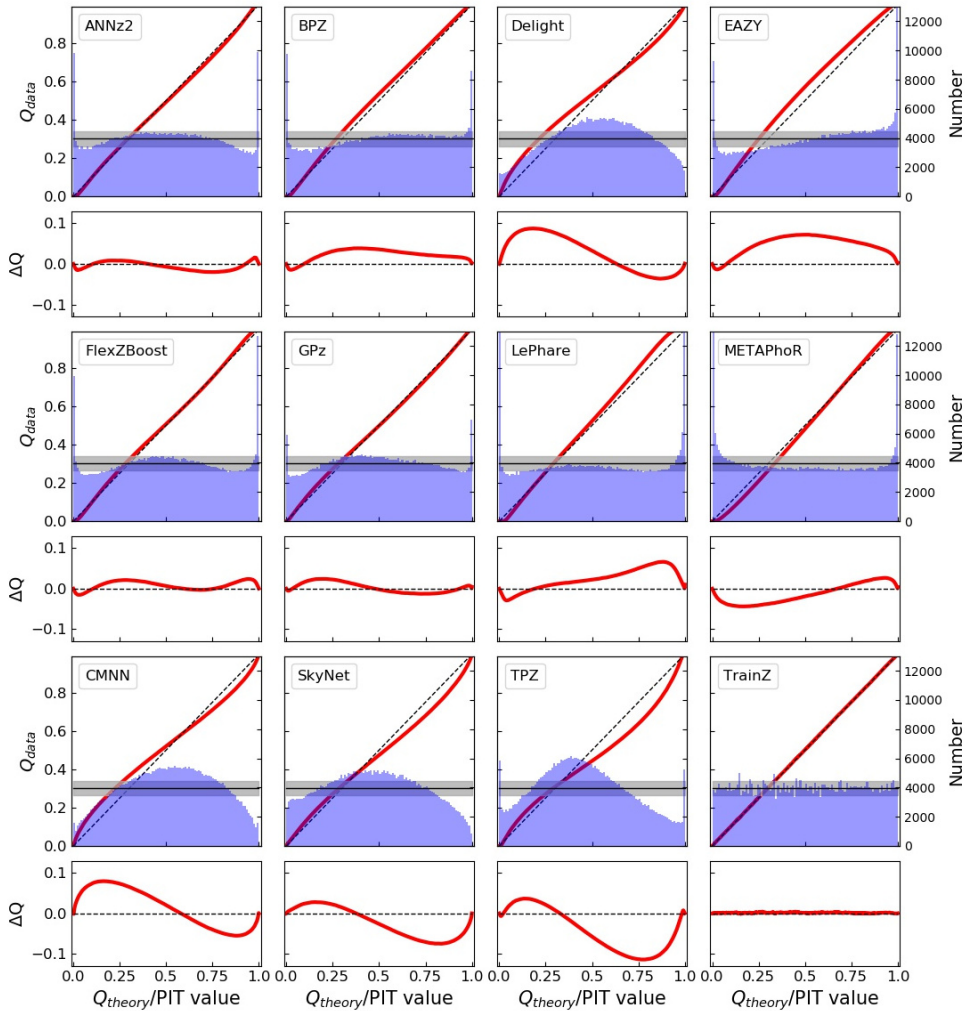


**Figure 2.** The QQ plot (red) and PIT histogram (blue) of the photo- $z$  PDF codes (panels) along with the ideal QQ (black dashed diagonal) and ideal PIT (gray horizontal) curves, as well as a difference plot for the QQ difference from the ideal diagonal (lower inset). The gray shaded region indicates the  $2\sigma$  range from a bootstrap resampling of the training set with a size of 30,000 galaxies using `trainZ`. The twelve codes exhibit varying degrees of four deviations from perfection: an overabundance of PIT values at the centre of the distribution indicate a catalogue of overly broad photo- $z$  PDFs, an excess of PIT values at the extrema indicates a catalogue of overly narrow photo- $z$  PDFs, catastrophic outliers manifest as overabundances at PIT values of 0 and 1, and asymmetry indicates systematic bias, a form of model misspecification. Values in excess of the  $2\sigma$  shaded region show that for some codes these errors will be significant given expected training sample sizes.

ment, the CDE Loss is the only metric that can appropriately penalize the pathological `trainZ`. Additionally, it favors CMNN and FlexZBoost, the latter of which is optimized for this metric.

comparison metrics. In Section 6.2, we outline the experiments we intend to build upon this study. In Section 6.3, we discuss the enhancements of the mock data set that will be necessary to enable the future experiments.

## 6 DISCUSSION AND FUTURE WORK

In contrast with other photo- $z$  PDF comparison papers that have aimed to identify the “best” code for a given survey, we have focused on the somewhat more philosophical questions of how to assess photo- $z$  PDF methods and how to interpret differences between codes in terms of photo- $z$  PDF performance. In Section 6.1, we reframe the strong performance of our pathological photo- $z$  PDF technique, `trainZ`, as a cautionary tale about the importance of choosing appropriate

### 6.1 Interpretation of metrics

We remind the reader that contributed codes were given a goal of obtaining accurate photo- $z$  PDFs, not an accurate stacked estimator of the redshift distribution, so we do not expect the same codes to necessarily perform well for both classes of metrics. Indeed, the codes were optimized for their interpretation of our request for “accurate photo- $z$  PDFs,” and we expect that the implementations would have been

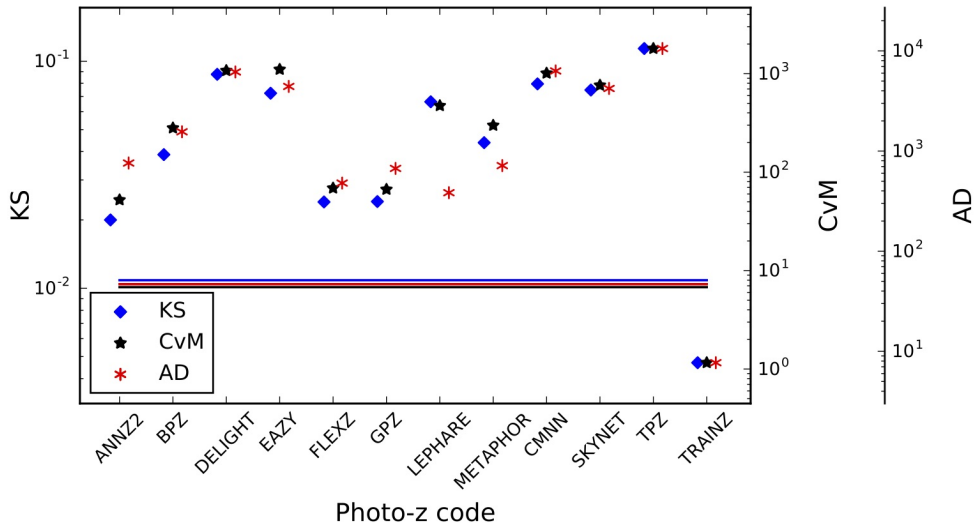


**Figure 3.** A visualization of the Kolmogorov-Smirnov (KS, blue diamond), Cramer-von Mises (CvM, black star), and Anderson-Darling (AD, red asterisk) statistics for the PIT distributions. There is generally good agreement between these statistics, with differences corresponding to the codes with outstanding catastrophic outlier rates, a reflection in the differences in how each statistic weights the tails of the distribution. Horizontal lines indicate the level of uncertainty found by bootstrapping a training set sample of 30,000 galaxies using `trainZ`; none of the codes reach this conservative ideal floor in expected uncertainty.

**Table 3.** CDE loss statistic of the individual photo- $z$  PDFs for each code. A lower value of the CDE loss indicates more accurate individual photo- $z$  PDFs, with CMNN and FlexZBoost performing best under this metric.

Photo- $z$ Code	CDE Loss
ANNz2	-6.88
BPZ	-7.82
Delight	-8.33
EAZY	-7.07
FlexZBoost	-10.60
GPz	-9.93
LePhare	-1.66
METAPhoR	-6.28
CMNN	-10.43
SkyNet	-7.89
TPZ	-9.55
<code>trainZ</code>	-0.83

adjusted had we requested optimization of the traditional metrics of Appendices A and B.

Furthermore, our metrics are not necessarily able to assess the fidelity of individual photo- $z$  PDFs relative to true posteriors: in the absence of a “true PDF” from which redshifts are drawn, it is difficult to construct metrics to measure performance for individual galaxies rather than ensembles. (The CDE Loss metric of section 4.2 is an exception to this rule.) A lack of appropriate metrics more sophisticated than the CDE Loss remains an open issue for science cases requiring accurate individual galaxy PDFs. The metric-specific performance demonstrated in this paper implies that we may need multiple photo- $z$  PDF approaches tuned to each metric in order to maximize returns over all science cases in large upcoming surveys.

The `trainZ` estimator of Section 3.3, which assigns every galaxy a photo- $z$  PDF equal to  $N(z)$  of the training

set, is introduced as an experimental control or null test to demonstrate this point via *reductio ad absurdum*. Because our training set is perfectly representative of the test set,  $N(z)$  should be identical for both sets down to statistical noise. **We make the alarming observation that `trainZ`, the experimental control, outperforms all codes on the CDF-based metrics, and all but one code on the  $N(z)$  based statistics.** The PIT and other CDF-based metrics upon which modern photo- $z$  PDF comparisons are built (Bordoloi et al. 2010; Polsterer et al. 2016; Tanaka et al. 2018) can be gamed by a trivial estimator that yields only an affirmation of prior knowledge uninformed by the data. In other words, such ensemble metrics are not appropriate for the task of selecting photo- $z$  PDF codes for analysis pipelines.

The CDE loss and point estimate metrics appropriately penalize `trainZ`’s naivete. As shown in Appendix B, `trainZ` has identical  $ZPEAK$  and  $ZWEIGHT$  values for every galaxy, and thus the photo- $z$  point estimates are constant as a function of true redshift, i. e. a horizontal line at the mode and mean of the training set distribution respectively. The explicit dependence on the individual posteriors in the calculation of the CDE loss, described in Section 5.2, distinguishes this metric from those of the photo- $z$  PDF ensemble and stacked estimator of the redshift distribution, despite their prevalence in the photo- $z$  literature.

In summary, context is crucial to defend against deceptively strong performers such as `trainZ`; **the best photo- $z$  PDF method is the one that most effectively achieves our science goals**, not the one that performs best on a metric that does not reflect those goals. In the absence of a single scientific motivation or the information necessary for a principled metric definition, we must consider many metrics and be critical of the information transmitted by each.

## 1047 6.2 Extensions to the experimental design

1048 The work presented in this paper is only a first step in as-  
 1049 sessing photo- $z$  PDF approaches and moving toward an im-  
 1050 proved photometric redshift estimator. Here we discuss the  
 1051 next steps for subsequent investigations.

1052 This initial paper explores photo- $z$  PDF code perfor-  
 1053 mance in idealized conditions with perfect catalog-based  
 1054 photometry and representative training data, but the re-  
 1055 silience of each code to such realistic imperfections in prior  
 1056 information has not yet been evaluated. A top priority for a  
 1057 follow-up study is to test realistic forms of incomplete, er-  
 1058 roneous, and non-representative template libraries and train-  
 1059 ing sets as well as the impact of other forms of external  
 1060 priors that must be ingested by the codes, major concerns  
 1061 in Newman et al. (2015); Masters et al. (2017). Outright red-  
 1062 shift failures due to emission line misidentification or noise  
 1063 spikes may be modeled by the inclusion of a small number  
 1064 of high-confidence yet false redshifts. We plan to perform a  
 1065 full sensitivity analysis on a realistically incomplete training  
 1066 set of spectroscopic galaxies, modeling the performance of  
 1067 spectrographs, emission-line properties, and expected signal-  
 1068 to-noise to determine which potential training set galaxies  
 1069 are most likely to be excluded.

1070 Appendix A only addresses the stacked estimator of the  
 1071 redshift distribution of the entire galaxy catalogue rather  
 1072 than subsets in bins, tomographic or otherwise. The effects  
 1073 of tomographic binning scheme will be explored in a dedi-  
 1074 cated future paper, including propagation of redshift uncer-  
 1075 tainties in a set of fiducial tomographic redshift bins in order  
 1076 to estimate impact on cosmological parameter estimation.

1077 Sequels to this study will also address some shortcom-  
 1078 ings of our experimental procedure. The fixed redshift grid  
 1079 shared between the codes may have unfairly penalized codes  
 1080 with a different native parameterization, as precision is lost  
 1081 when converting between formats. Performance on the (ad-  
 1082 mittedly small) population of sharply peaked photo- $z$  PDFs  
 1083 may have been suppressed across all codes due to the insuffi-  
 1084 cient resolution of the redshift grid. In light of the results of  
 1085 Malz et al. (2018), in future analyses we plan to switch from  
 1086 a fixed grid to the quantile parameterization or to permit  
 1087 each code to use its native storage format under a shared  
 1088 number of parameters.

1089 Section 4 discussed the difficulty in evaluating PDF ac-  
 1090 curacy for individual objects. In a follow-up study, we will  
 1091 generate “true PDF” distributions, yielding a dataset that  
 1092 enables a test of PDF accuracy for individual galaxies rather  
 1093 than solely ensembles.

## 1094 6.3 Realistic mock data

1095 To make optimal use of the LSST data for cosmological  
 1096 and other astrophysical analyses of the LSST-DESC Sci-  
 1097 ence Roadmap, future investigations that build upon this  
 1098 one will require a more sophisticated set of galaxy photome-  
 1099 try and redshifts. This initial paper explored a data set that  
 1100 was constructed at the catalog level, with no inclusion of the  
 1101 complications that come from measuring photometry from  
 1102 images. Future data challenges will move to catalogs con-  
 1103 structed from mock images, including the complications of  
 1104 deblending, sensor inefficiencies, and heterogeneous observ-

1105 ing conditions, all anticipated to affect the measured colours  
 1106 of LSST’s galaxy sample (Dawson et al. 2016).

1107 The DC1 galaxy SEDs were linear combinations of just  
 1108 five basis SED templates, but a next generation of data for  
 1109 photo- $z$  PDF investigations must include a broader range of  
 1110 physical properties. Though we only considered  $z < 2$  here,  
 1111 LSST 10-year data will contain  $z > 2$  galaxies, plagued by  
 1112 fainter apparent magnitudes and anomalous colours due to  
 1113 stellar evolution. A subsequent study must also have a data  
 1114 set that includes low-level active galactic nuclei (AGN) fea-  
 1115 tures in the SEDs, which perturb colours and other host  
 1116 galaxy properties. An observational degeneracy between the  
 1117 Lyman break of a  $z \sim 2 - 3$  galaxy from the Balmer break  
 1118 of a  $z \sim 0.2 - 0.3$  galaxy is a known source of catastrophic  
 1119 outliers (Massarotti et al. 2001) that was not effectively in-  
 1120 cluded in this study. To gauge the sensitivity of photo- $z$   
 1121 PDF estimators to catastrophic outliers, our data set must  
 1122 include realistic high-redshift galaxy populations.

1123 The overarching plan describing everything laid out in  
 1124 this section is described in more detail in the LSST-DESC  
 1125 Science Roadmap (see Footnote in Section 1).

## 7 CONCLUSION

1126 This paper compares twelve photo- $z$  PDF codes under con-  
 1127 trolled experimental conditions of representative and com-  
 1128 plete prior information to set a baseline for an upcoming  
 1129 sensitivity analysis. This work isolates the impact on met-  
 1130 rics of photo- $z$  PDF accuracy due to the estimation tech-  
 1131 nique as opposed to the complications of realistic physical  
 1132 systematics of the photometry. Though the mock data set of  
 1133 this investigation did not include true photo- $z$  posteriors for  
 1134 comparison, we interpret deviations from perfect re-  
 1135 sults given perfect prior information as the imprint  
 1136 of the implicit assumptions underlying the estima-  
 1137 tion approach.

1138 We evaluate the twelve codes under science-agnostic  
 1139 metrics both established and emerging to stress-test the  
 1140 ensemble properties of photo- $z$  PDF catalogues derived by  
 1141 each method. In appendices, we also present metrics of point  
 1142 estimates and a prevalent summary statistic of photo- $z$  PDF  
 1143 catalogues used in cosmological analyses to enable the reader  
 1144 to relate this work to studies of similar scope. We observe  
 1145 that no one code dominates in all metrics, and that the stan-  
 1146 dard metrics of photo- $z$  PDFs and the stacked estimator of  
 1147 the redshift distribution can be gamed by a very simplistic  
 1148 procedure that asserts the prior over the data. We empha-  
 1149 size to the photo- $z$  community that metrics used to vet  
 1150 photo- $z$  PDF methods must be scrutinized to ensure  
 1151 they correspond to the quantities that matter to our  
 1152 science.

## 1153 Acknowledgments

1154 Author contributions are listed below.

S.J. Schmidt: Co-led the project. (conceptualization, data  
 1155 curation, formal analysis, investigation, methodology,  
 1156 project administration, resources, software, supervision,  
 1157 visualization, writing – original draft, writing – review &  
 1158 editing)

A.I. Malz: Co-led the project, contributed to choice of

metrics, implementation in code, and writing. (conceptualization, methodology, project administration, resources, software, visualization, writing – original draft, writing – review & editing) J.Y.H. Soo: Ran ANNz2 and Delight, updated abstract, edited sections 1 through 6, added tables in Methods and Results, updated references.bib and added references throughout the paper I.A. Almosallam: vetted the early versions of the data set and ran many photo-z codes on it, applied GPz to the final version and wrote the GPz subsection M. Brescia: main ideator of METAPHOR and of MLPQNA; modification of METAPHOR pipeline to fit the LSST data structure and requirements S. Cavuoti: Contributed to choice and test of metrics, ran METAPHOR, minor text editing J. Cohen-Tanugi: contributed to running code, analysis discussion, and editing, reviewing the paper A.J. Connolly: Developed the colour-matched nearest-neighbours photo-z code; participated in discussions of the analysis. P.E. Freeman: Contributed to choice of CDE metrics and to implementation of FlexZBoost M.L. Graham: Ran the colour-matched nearest-neighbours photo-z code on the Buzzard catalog and wrote the relevant piece of Section 2; participated in discussions of the analysis. K. Iyer: assisted in writing metric functions used to evaluate codes M.J. Jarvis: Contributed text on AGN to Discussion section and portions of GPz work J.B. Kalmbach: Worked on preparing the figures for the paper. E. Kovacs: Ran simulations, discussed data format and properties for SEDs, dust, and ELG corrections A.B. Lee: Co-developed FlexZBoost and the CDE loss statistic, wrote text on the work, and supervised the development of FlexZBoost software packages G. Longo: Scientific advise, test and validation of the modified METAPHOR pipeline, text of the METAPHOR section C. B. Morrison: Managerial support; Discussions with authors regarding metrics and style; Some coding contribution to metric computation. J. Newman: Contributions to overall strategy, design of metrics, and supervision of work done by Rongpu Zhou E. Nourbakhsh: Ran and optimized TPZ code and wrote a subsection of Section 2 for TPZ E. Nuss: contributed to running code, analysis discussion, and editing, reviewing the paper T. Pospisil: Co-developed FlexZBoost software and CDE loss calculation code H. Tranin: contributed to providing SkyNet results and writing the relevant section R. Zhou: Optimized and ran EAZY and contributed to the draft R. Izbicki: Co-developed FlexZBoost and the CDE loss statistic, and wrote software for FlexZBoost

The authors would like to thank their LSST-DESC publication review committee for comments that improved the paper draft.

**personal funding sources** SJS acknowledges support

from DOE grant DE-SC0009999 and NSF/AURA grant N56981C. AIM acknowledges support from the Max Planck Society and the Alexander von Humboldt Foundation in the framework of the Max Planck-Humboldt Research Award endowed by the Federal Ministry of Education and Research. During the completion of this work, AIM was advised by David W. Hogg and was supported by National Science Foundation grant AST-1517237.

In addition to packages cited in the text, analyses performed in this paper used the following software packages: `Numpy` and `Scipy` ([Oliphant 2007](#)), `Matplotlib` ([Hunter 2007](#)), `Seaborn` ([Waskom et al. 2017](#)), `minFunc` ([Schmidt 2005](#)), `qp` ([Malz & Marshall 2018; Malz et al. 2018](#)), `pySkyNet` ([Bonnett 2016](#)), and `photUtils` from the LSST simulations package ([Connolly et al. 2014](#)).

The DESC acknowledges ongoing support from the Institut National de Physique Nucléaire et de Physique des Particules in France; the Science & Technology Facilities Council in the United Kingdom; and the Department of Energy, the National Science Foundation, and the LSST Corporation in the United States. DESC uses resources of the IN2P3 Computing Center (CC-IN2P3-Lyon/Villeurbanne - France) funded by the Centre National de la Recherche Scientifique; the National Energy Research Scientific Computing Center, a DOE Office of Science User Facility supported by the Office of Science of the U.S. Department of Energy under Contract No. DE-AC02-05CH11231; STFC DiRAC HPC Facilities, funded by UK BIS National E-infrastructure capital grants; and the UK particle physics grid, supported by the GridPP Collaboration. This work was performed in part under DOE Contract DE-AC02-76SF00515.

## APPENDIX A: EVALUATION OF THE REDSHIFT DISTRIBUTION

Perhaps the most popular application of photo-z PDFs is the estimation of the overall redshift distribution  $N(z)$ , a quantity that enters some cosmological calculations and the true value of which is known for the DC1 data set and will be denoted as  $\tilde{N}(z)$ . In terms of the prior information provided to each method, the true redshift distribution satisfies the tautology  $\tilde{N}(z) = p(z|I_D)$  due to our experimental set-up; because the DC1 training and template sets are representative and complete,  $I_D$  represents a prior that is also equal to the truth. In this ideal case of complete and representative prior information, the method that would give the best approximation to  $\tilde{N}(z)$  would be one that neglects all the information contained in the photometry  $\{d_i\}_{N_{tot}}$  and gives every galaxy the same photo-z PDF  $\hat{p}_i(z) = \tilde{N}(z)$  for all  $i$ ; the inclusion of any information from the photometry would only introduce noise to the optimal result of returning the prior. This is the exact estimator, `trainZ`, that we have described in Section 3.3, and which will serve as an experimental control.

1276 **A1 Metrics of the stacked estimator of the  
1277 redshift distribution**

1278 “Stacking” according to

$$1279 \hat{N}^H(z) \equiv \frac{1}{N_{tot}} \sum_i^{N_{tot}} \hat{p}_i^H(z) \quad (A1) \quad 1336$$

1280 is the most widely accepted method for obtaining  $\hat{N}^H(z)$  as  
1281 an estimator of the redshift distribution from photo- $z$  PDFs  
1282 derived by a method  $H$ . Though the use of the stacked es-  
1283 timator of the redshift distribution is not formally correct  
1284 ([Malz & Hogg prep](#)), we use it under the untested assump-  
1285 tion that the response of our metrics of  $\hat{N}^H(z)$  will be anal-  
1286 ogous to the same metrics applied to a principled estimator  
1287 of the redshift distribution.

1288 As  $N(z)$  is itself a univariate PDF, we apply the met-  
1289 rics of the previous sections to it as well. We additionaly  
1290 calculate the first three moments

$$1291 \langle z^m \rangle \equiv \int_{-\infty}^{\infty} z^m N(z) dz \quad (A2) \quad 1350$$

1292 of the estimated redshift distribution  $\hat{N}^H(z)$  for each code  
1293 and compare them to the moments of the true redshift distri-  
1294 bution  $\tilde{N}(z)$ . Under the assumption that the stacked estima-  
1295 tor is unbiased, a superior method minimizes the difference  
1296 between the true and estimated moments.

1297 **A2 Performance on the stacked estimator of the  
1298 redshift distribution**

1299 Figure A1 shows the stacked estimator  $\hat{N}(z)$  of the redshift  
1300 distribution for each code compared to the true redshift  
1301 distribution  $\tilde{N}(z)$ , where the stacked estimator has been  
1302 smoothed for each code in the plot using a kernel density  
1303 estimate (KDE) with a bandwidth chosen by Scott’s Rule  
1304 ([Scott 1992](#)) in order to minimize visual differences in small-  
1305 scale features; the quantitative statistics, however, are calcu-  
1306 lated using the empirical CDF which is not smoothed.

1307 Many of the codes, including all the model-fitting ap-  
1308 proaches and ANNz2, GPz, METAPhoR, and SkyNet from the  
1309 data-driven camp, overestimate the redshift density at  $z \sim$   
1310 1.4. This behavior is a consequence of the 4000 Åbreak pass-  
1311 ing through the gap between the  $z$  and  $y$  filters, which in-  
1312 duces a genuine discontinuity in the  $z-y$  colour as a function  
1313 of redshift that can sway the photo- $z$  PDF estimates in the  
1314 absence of bluer spectral features.

1315 ANNz2, GPz, and METAPhoR feature exaggerated peaks  
1316 and troughs relative to the training set, a potential sign  
1317 of overtraining. Further investigation on overtraining is  
1318 needed, if present this is an obstacle that may be overcome  
1319 with adjustment of the implementation.

1320 As expected, trainZ perfectly recovers the true redshift  
1321 distribution: as the training sample is selected from the same  
1322 underlying distribution as the test set, the redshift distribu-  
1323 tions are identical, up to Poisson fluctuations due to the  
1324 finite number of sample galaxies. CMNN is also in excellent  
1325 agreement for similar reasons: with a representative train-  
1326 ing sample of galaxies spanning the colour-space, the sum  
1327 of the colour-matched neighbour redshifts should return the  
1328 true redshift distribution. FlexZBoost and TPZ also perform  
1329 superb recovery of the true redshift distribution, with only  
1330 a slight deviation at  $z \sim 1.4$ . Our metrics, however, cannot

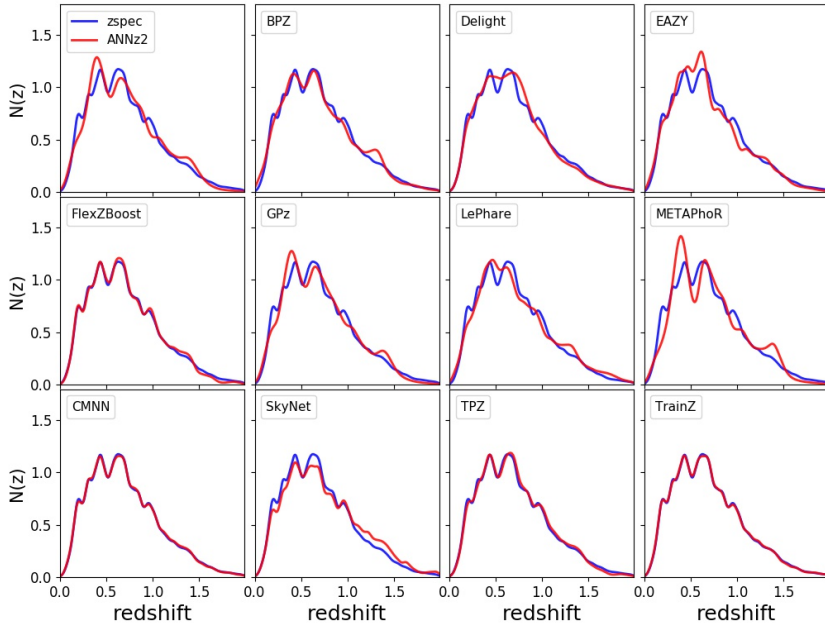
1331 discern whether these four approaches, as well as Delight,  
1332 are spared the  $z \sim 1.4$  degeneracy in  $\hat{N}(z)$  because they have  
1333 more effectively used information in the data or if the impact  
1334 is simply washed out by the stacked estimator’s effective av-  
1335 erage over the test set galaxy sample. See Appendix B for  
1336 further discussion of the  $z \sim 1.4$  issue.

Figure A2 shows the quantitative Kolmogorov-Smirnoff  
(KS), Cramer-Von Mises (CvM), and Anderson Darling  
(AD) test statistics for each of the codes for the  $\hat{N}(z)$  based  
measures. The horizontal lines show the the result of a boot-  
strap resampling of the training set using 30,000 samples for  
trainZ, representing a conservative idealized limit on ex-  
pected performance for a modest-sized representative training  
set of galaxies, as mentioned in Section 5.1. The AD  
bootstrap statistic is elevated due to its sensitivity to the  
tails of distributions. The stacked estimators of the redshift  
distribution for CMNN and trainZ best estimate  $\tilde{N}(z)$  under  
these metrics, whereas EAZY, LePhare, METAPhoR, and  
SkyNet underperform; BPZ, GPz, and TPZ are within a factor  
of two of the conservative limit for all statistics. It is un-  
surprising that CMNN scores well, as with a nearly complete  
and representative training set choosing neighbouring points  
in color/magnitude space to construct an estimator should  
lead to excellent agreement in the final  $\hat{N}(z)$ .

It is, however, surprising that TPZ does well on  $\hat{N}(z)$   
given its poor performance on the ensemble photo- $z$  PDFs,  
especially knowing that TPZ was optimized for photo- $z$  PDF  
ensemble metrics rather than the stacked estimator of the  
redshift distribution. A possible explanation is the choice of  
smoothing parameter chosen during validation, which affects  
photo- $z$  PDF widths as well as overall redshift bias and could  
be modified to improve performance under the photo- $z$  PDF  
metrics.

We calculated the first three moments of the stacked  
 $\hat{N}(z)$  distribution of all galaxies and compared it to the mo-  
ments of the true redshift distribution. Figure A3 shows the  
residuals of the moments for all codes. Accuracy of the  
moments varies widely between codes, raising concerns about  
the propagation to cosmological analyses. The DESC SRD  
([The LSST Dark Energy Science Collaboration et al. 2018](#))  
lists stringent requirements on how well the mean and varian-  
ce of tomographic redshift bins must be known for each  
of the main DESC science cases. We indicate the Year 1 re-  
quirements assuming our true mean redshift of  $z = 0.701$  as  
dashed lines. In this study with representative training data,  
ANNz2, BPZ, CMNN, TPZ, and our pathological trainZ estima-  
tor meet the Y1 requirement on the mean redshift. Only  
ANNz2, BPZ, CMNN, and trainZ meet both requirements. One  
should be concerned that many codes fail to meet this ambi-  
tious limit under perfect prior information because all codes  
are anticipated to do no better under realistically imperfect  
prior information, and indicates that additional calibration  
to remove these systematic offsets (e.g. [Newman 2008](#)) will  
likely be necessary in order to meet these stringent goals.

SkyNet exhibits redshift bias in Figure A1 and is a clear  
outlier in the first moment of  $\hat{N}(z)$  in Figure A3. The SkyNet  
algorithm employs a random subsampling of the training  
set without testing that the subset is representative of the  
full population, and the implementation used here does not  
upweight rarer low- and high-redshift galaxies, as in [Bonnett  
\(2015\)](#), suggesting a possible cause that may be addressed  
in future work.



**Figure A1.** The smoothed stacked estimator  $\hat{N}(z)$  of the redshift distribution (red) produced by each code (panels) compared to the true redshift distribution  $\tilde{N}(z)$  (blue). Varying levels of agreement are seen among the codes, with the smallest deviations for CMNN, FlexZBoost, TPZ, and trainZ.

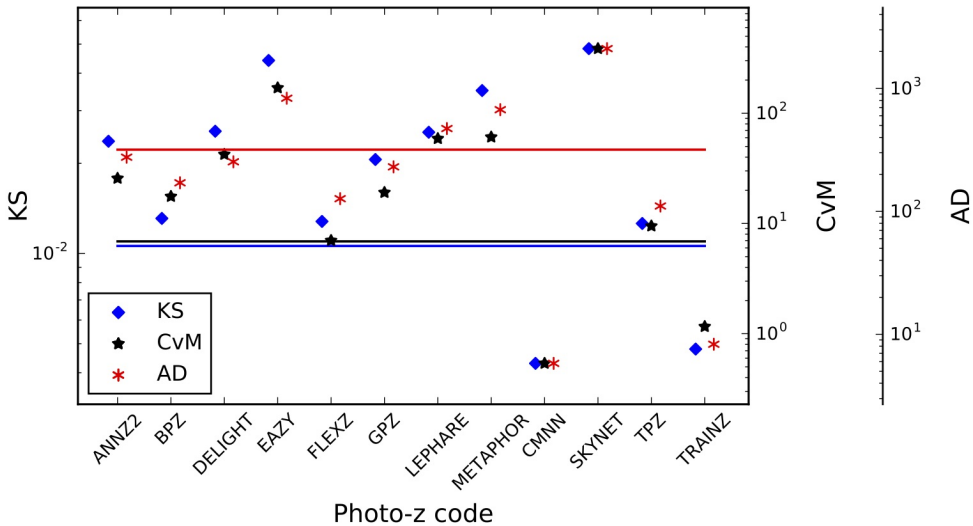


**Figure A2.** A visualization of the Kolmogorov-Smirnov (KS, blue diamond), Cramer-von Mises (CvM, black star), and Anderson-Darling (AD, red asterisk) statistics for the  $\hat{N}(z)$  distributions. Horizontal lines indicate the statistic values (including uncertainty) achieved using trainZ via bootstrap resampling a training set containing 30,000 redshifts. We make the reassuring observation that these related statistics do not disagree significantly with one another. CMNN outperforms the control case, trainZ, and several codes are within a factor of two of this conservative idealized limit. SkyNet scores poorly due to an overall bias in its redshift predictions.

1393 APPENDIX B: Photo- $z$  POINT ESTIMATION  
1394 AND METRICS

1398 dual diagnostic tool and to facilitate direct comparisons to  
1399 historical studies.

1395 While this work assumes that science applications value the  
1396 information of the full photo- $z$  PDF, we present conventional  
1397 metrics of photo- $z$  point estimates as a quick and dirty vi-

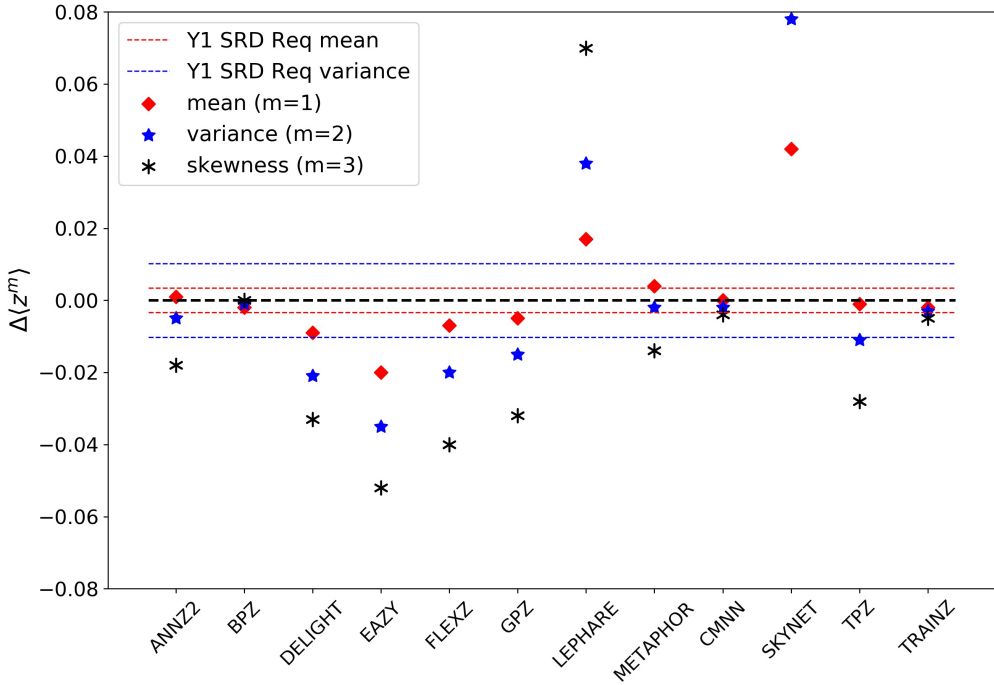


**Figure A3.** Residuals of the first three moments of the stacked  $\hat{N}(z)$  distribution. Red and blue horizontal lines indicate the Year 1 DESC SRD requirements on accuracy of the mean and variance respectively. Only a small number of codes are able to meet these specifications even with perfect training data.

### B1 Reduction of photo- $z$ PDFs to point estimates

Though we acknowledge that many of the codes can also return a native photo- $z$  point estimate, we put all codes on equal footing by considering two generic photo- $z$  point estimators, the mode  $z_{PEAK}$  and main-peak-mean  $z_{WEIGHT}$  (Dahlen et al. 2013), a weighted mean within the bounds of the main peak, as identified by the roots of  $p(z) - 0.05 \times z_{PEAK}$ . Though  $z_{WEIGHT}$  neglects information in a secondary peak of e. g. a bimodal distribution, it avoids the pitfall of reducing the photo- $z$  PDF to a redshift between peaks where there is low probability.

### B2 Metrics of photo- $z$ point estimates

We calculate the commonly used point estimate metrics of the overall intrinsic scatter, bias, and catastrophic outlier rate, defined in terms of the standard error  $e_z \equiv (z_{PEAK} - z_{true})/(1 + z_{true})$ . Because the standard deviation of the photo- $z$  residuals is sensitive to outliers, we define the scatter in terms of the Interquartile Range (IQR), the difference between the 75th and 25th percentiles of the distribution of  $e_z$ , imposing the scaling  $\sigma_{IQR} = IQR/1.349$  to ensure that the area within  $\sigma_{IQR}$  is the same as that within one standard deviation from a standard Normal distribution. We also resist the effect of catastrophic outliers by defining the bias  $b_z$  as the median rather than mean value of  $e_z$ . The catastrophic outlier rate  $f_{out}$  is defined as the fraction of galaxies with  $e_z$  greater than  $\max(3\sigma_{IQR}, 0.06)$ .

For reference, Section 3.8 of the LSST Science Book (Abell et al. 2009) uses the standard definitions of these parameters in requiring

- RMS scatter  $\sigma < 0.02(1 + z_{true})$

- bias  $b_z < 0.003$
- catastrophic outlier rate  $f_{out} < 10\%$ .

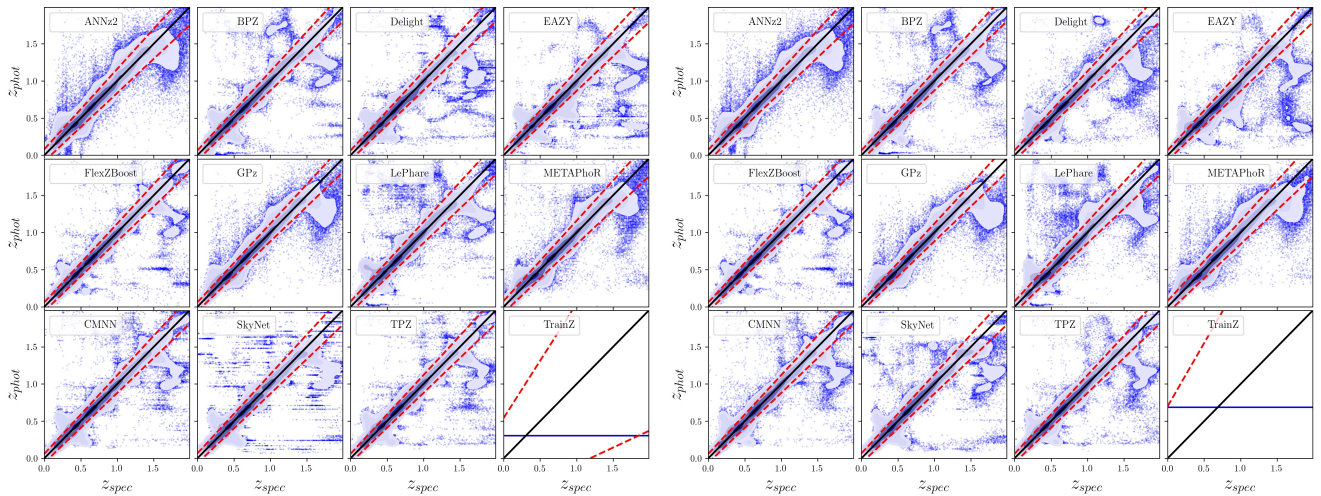
### B3 Comparison of photo- $z$ point estimate metrics

Figure B1 shows both point estimates for all codes both  $z_{PEAK}$  and  $z_{WEIGHT}$ . Point density is shown with mixed contours to emphasize that most of the galaxies do fall close to the  $z_{phot} = z_{spec}$  line, while points trace the details of the catastrophic outlier populations.

The finite grid spacing of the photo- $z$  PDFs induces some discretization in  $z_{PEAK}$ . The features perpendicular to the  $z_{phot} = z_{spec}$  line are due to the 4000 Åbreak passing through the gaps between adjacent filters. Even the strongest codes feature populations far from the  $z_{phot} = z_{spec}$  line representing a degeneracy in the space of colours and redshifts.

The intrinsic scatter, bias, and catastrophic outlier rate are given in Table B1. Perhaps unsurprisingly, performance under these metrics largely tracks that of the metrics of Section 4 of the photo- $z$  PDFs from which the point estimates were derived. All twelve codes perform at or near the goals of the LSST Science Requirements Document<sup>18</sup> and Graham et al. (2018), which is encouraging if not unexpected for  $i < 25.3$ .

<sup>18</sup> available at: <http://ls.st/srd>



**Figure B1.** The density of photo- $z$  point estimates (contours) reduced from the photo- $z$  PDFs with outliers (blue) beyond the outlier cutoff (red dashed lines), via the mode ( $z_{PEAK}$ , left panel) and main-peak-mean ( $z_{WEIGHT}$ , right panel). The **trainZ** estimator (lower right sub-panels) has a shared  $z_{PEAK}$  and  $z_{WEIGHT}$  for the entire test set galaxy sample.

**Table B1.** Photo- $z$  point estimate statistics

Photo- $z$ PDF Code	$Z_{PEAK}$		$Z_{WEIGHT}$			
	$\sigma_{IQR}/(1+z)$	median	outlier fraction	$\sigma_{IQR}/(1+z)$	median	outlier fraction
ANNz2	0.0270	0.00063	0.044	0.0244	0.000307	0.047
BPZ	0.0215	-0.00175	0.035	0.0215	-0.002005	0.032
Delight	0.0212	-0.00185	0.038	0.0216	-0.002158	0.038
EAZY	0.0225	-0.00218	0.034	0.0226	-0.003765	0.029
FlexZBoost	0.0154	-0.00027	0.020	0.0148	-0.000211	0.017
GPz	0.0197	-0.00000	0.052	0.0195	0.000113	0.051
LePhare	0.0236	-0.00161	0.058	0.0239	-0.002007	0.056
METAPhoR	0.0264	0.00000	0.037	0.0262	0.001333	0.048
CMNN	0.0184	-0.00132	0.035	0.0170	-0.001049	0.034
SkyNet	0.0219	-0.00167	0.036	0.0218	0.000174	0.037
TPZ	0.0161	0.00309	0.033	0.0166	0.003048	0.031
<b>trainZ</b>	0.1808	-0.2086	0.000	0.2335	0.022135	0.000

## REFERENCES

- Abbott T., et al., 2005, preprint (arXiv:astro-ph/0510346)  
 Abell P. A., et al., 2009, preprint (arXiv:0912.0201),  
 Aihara H., et al., 2018a, *PASJ*, **70**, S4  
 Aihara H., et al., 2018b, *PASJ*, **70**, S8  
 Almosallam I. A., Lindsay S. N., Jarvis M. J., Roberts S. J., 2016a, *MNRAS*, **455**, 2387  
 Almosallam I. A., Jarvis M. J., Roberts S. J., 2016b, *MNRAS*, **462**, 726  
 Arnouts S., Cristiani S., Moscardini L., Matarrese S., Lucchin F., Fontana A., Giallongo E., 1999, *MNRAS*, **310**, 540  
 Behroozi P. S., Wechsler R. H., Wu H.-Y., 2013, *ApJ*, **762**, 109  
 Benítez N., 2000, *ApJ*, **536**, 571  
 Bernstein G., Huterer D., 2010, *MNRAS*, **401**, 1399  
 Blanton M. R., Roweis S., 2007, *AJ*, **133**, 734  
 Blanton M. R., et al., 2005, *AJ*, **129**, 2562  
 Bonnett C., 2015, *MNRAS*, **449**, 1043  
 Bonnett C., 2016, Python wrapper to SkyNet, <https://pyskynet.readthedocs.io/en/latest/>  
 Bonnett C., et al., 2016, *Phys. Rev. D*, **94**, 042005  
 Bordoloi R., Lilly S. J., Amara A., 2010, *MNRAS*, **406**, 881  
 Brammer G. B., van Dokkum P. G., Coppi P., 2008, *ApJ*, **686**, 1503  
 Breiman L., Friedman J. H., Olshen R. A., Stone C. J., 1984, Classification and Regression Trees, Statistics/Probability Series. Wadsworth Publishing Company, Belmont, California, U.S.A  
 Brescia M., Cavuoti S., Amaro V., Riccio G., Angora G., Vellucci C., Longo G., 2018, preprint, ([arXiv:1802.07683](https://arxiv.org/abs/1802.07683))  
 Carrasco Kind M., Brunner R. J., 2013, *MNRAS*, **432**, 1483  
 Carrasco Kind M., Brunner R. J., 2014, *MNRAS*, **442**, 3380  
 Cavuoti S., Amaro V., Brescia M., Vellucci C., Tortora C., Longo G., 2017, *MNRAS*, **465**, 1959  
 Chen T., Guestrin C., 2016, in Proceedings of the 22Nd ACM SIGKDD International Conference on Knowledge Discovery and Data Mining. KDD '16. ACM, New York, NY, USA, pp 785–794, doi:10.1145/2939672.2939785, <http://doi.acm.org/10.1145/2939672.2939785>  
 Connolly A. J., et al., 2014, in Angeli G. Z., Dierickx P., eds, Society of Photo-Optical Instrumentation Engineers (SPIE) Conference Series Vol. 9150, Modeling, Systems Engineering, and Project Management for Astronomy VI. p. 14, doi:10.1117/12.2054953

- 1495 Dahlen T., et al., 2013, *ApJ*, **775**, 93  
 1496 Dawson W. A., Schneider M. D., Tyson J. A., Jee M. J., 2016,  
   *ApJ*, **816**, 11  
 1498 DeRose J., et al., 2019, arXiv e-prints, p. [arXiv:1901.02401](https://arxiv.org/abs/1901.02401)  
 1499 Erben T., et al., 2013, *MNRAS*, **433**, 2545  
 1500 Fernández-Soto A., Lanzetta K. M., Yahil A., 1999, *ApJ*, **513**, 34  
 1501 Firth A. E., Lahav O., Somerville R. S., 2003, *MNRAS*, **339**, 1195  
 1502 Freeman P. E., Izbicki R., Lee A. B., 2017, *MNRAS*, **468**, 4556  
 1503 Graff P., Feroz F., Hobson M. P., Lasenby A., 2014, *MNRAS*, **441**,  
   1741  
 1504 Graham M. L., Connolly A. J., Ivezić Ž., Schmidt S. J., Jones  
   R. L., Jurić M., Daniel S. F., Yoachim P., 2018, *AJ*, **155**, 1  
 1506 Green J., et al., 2012, preprint (arXiv:1208.4012),  
 1507 Hildebrandt H., et al., 2010, *A&A*, **523**, A31  
 1509 Hofmann B., Mathé P., 2018, *Inverse Problems*, **34**, 015007  
 1510 Hunter J. D., 2007, Matplotlib: A 2D Graphics Environment,  
   doi:[10.1109/MCSE.2007.55](https://doi.org/10.1109/MCSE.2007.55)  
 1512 Ilbert O., et al., 2006, *A&A*, **457**, 841  
 1513 Ivezić Ž., et al., 2008, preprint (arXiv:0805.2366),  
 1514 Izbicki R., Lee A. B., 2017, *Electron. J. Statist.*, **11**, 2800  
 1515 Izbicki R., Lee A. B., Freeman P. E., 2017, *Ann. Appl. Stat.*, **11**,  
   698  
 1517 Laureijs R., et al., 2011, preprint (1110.3193),  
 1518 Leistedt B., Hogg D. W., 2017, *ApJ*, **838**, 5  
 1519 Malz A., Hogg D., in prep., CHIPPR, chippr, <https://github.com/aimalz/chippr>  
 1521 Malz A., Marshall P., 2018, qp: Quantile parametrization for  
   probability distribution functions (ascl:1809.011)  
 1523 Malz A. I., Marshall P. J., DeRose J., Graham M. L., Schmidt  
   S. J., Wechsler R., (LSST Dark Energy Science Collaboration  
   2018, *AJ*, **156**, 35  
 1526 Mandelbaum R., et al., 2008, *MNRAS*, **386**, 781  
 1527 Massarotti M., Iovino A., Buzzoni A., 2001, *A&A*, **368**, 74  
 1528 Masters D. C., Stern D. K., Cohen J. G., Capak P. L., Rhodes  
   J. D., Castander F. J., Paltani S., 2017, *ApJ*, **841**, 111  
 1530 Newman J. A., 2008, *ApJ*, **684**, 88  
 1531 Newman J. A., et al., 2015, *Astroparticle Physics*, **63**, 81  
 1532 Oliphant T., 2007, Python for Scientific Computing,  
   doi:[10.1109/MCSE.2007.55](https://doi.org/10.1109/MCSE.2007.55)  
 1534 Oyaizu H., Lima M., Cunha C. E., Lin H., Frieman J., 2008, *ApJ*,  
   689, 709  
 1536 Polsterer K. L., D'Isanto A., Gieseke F., 2016, preprint  
   (arXiv:1608.08016),  
 1538 Rasmussen C., Williams C., 2006, Gaussian Processes for Machine  
   Learning. Adaptative computation and machine learning se-  
   ries, MIT Press, Cambridge, MA  
 1541 Rau M. M., Seitz S., Brimioule F., Frank E., Friedrich O., Gruen  
   D., Hoyle B., 2015, *MNRAS*, **452**, 3710  
 1543 Reddick R. M., Wechsler R. H., Tinker J. L., Behroozi P. S., 2013,  
   *ApJ*, **771**, 30  
 1545 Sadeh I., Abdalla F. B., Lahav O., 2016, *PASP*, **128**, 104502  
 1546 Sánchez C., et al., 2014, *MNRAS*, **445**, 1482  
 1547 Schmidt M., 2005, minFunc: Unconstrained Differentiable Mul-  
   tivariate Optimization in Matlab, <http://www.cs.ubc.ca/~schmidtm/Software/minFunc.html>  
 1550 Scott D. W., 1992, Multivariate Density Estimation. Theory,  
   Practice, and Visualization. Wiley  
 1552 Sheldon E. S., Cunha C. E., Mandelbaum R., Brinkmann J.,  
 1553 Weaver B. A., 2012, *The Astrophysical Journal Supplement  
   Series*, **201**, 32  
 1555 Skrutskie M. F., et al., 2006, AJ, **131**, 1163  
 1556 Tanaka M., et al., 2018, *PASJ*, **70**, S9  
 1557 The LSST Dark Energy Science Collaboration et al., 2018,  
   preprint, ([arXiv:1809.01669](https://arxiv.org/abs/1809.01669))  
 1559 Waskom M., et al., 2017, doi:[10.5281/zenodo.824567](https://doi.org/10.5281/zenodo.824567)  
 1560 York D. G., et al., 2000, AJ, **120**, 1579  
 1561 de Jong J. T. A., Verdoes Kleijn G. A., Kuijken K. H., Valentijn  
   E. A., 2013, *Exp. Astron.*, **35**, 25  
 1563 de Jong J. T. A., et al., 2017, *A&A*, **604**, A134